



**HAL**  
open science

## Decoupling the Contributions of Different Instability Mechanisms to the PEMFC Performance Decay of Non-noble Metal O<sub>2</sub>-Reduction Catalysts

Seçil Ünsal, Robin Girod, Christian Appel, Dmitry Karpov, Michel Mermoux, Frédéric Maillard, Viktoriia A Saveleva, Vasiliki Tileli, Thomas J Schmidt, Juan Herranz

### ► To cite this version:

Seçil Ünsal, Robin Girod, Christian Appel, Dmitry Karpov, Michel Mermoux, et al.. Decoupling the Contributions of Different Instability Mechanisms to the PEMFC Performance Decay of Non-noble Metal O<sub>2</sub>-Reduction Catalysts. *Journal of the American Chemical Society*, 2023, 145 (14), pp.7845 - 7858. 10.1021/jacs.2c12751 . hal-04089928

**HAL Id: hal-04089928**

**<https://hal.science/hal-04089928v1>**

Submitted on 5 May 2023

**HAL** is a multi-disciplinary open access archive for the deposit and dissemination of scientific research documents, whether they are published or not. The documents may come from teaching and research institutions in France or abroad, or from public or private research centers.

L'archive ouverte pluridisciplinaire **HAL**, est destinée au dépôt et à la diffusion de documents scientifiques de niveau recherche, publiés ou non, émanant des établissements d'enseignement et de recherche français ou étrangers, des laboratoires publics ou privés.

# Decoupling the Contributions of Different Instability Mechanisms to the PEMFC Performance Decay of Non-noble Metal O<sub>2</sub>-reduction Catalysts

Seçil Ünsal<sup>a</sup>, Robin Girod<sup>b</sup>, Christian Appel<sup>c</sup>, Dmitry Karpov<sup>d</sup>, Michel Mermoux<sup>e</sup>, Frédéric Maillard<sup>e</sup>, Viktoriia A. Saveleva<sup>f</sup>, Vasiliki Tileli<sup>b</sup>, Thomas J. Schmidt<sup>a,g</sup>, Juan Herranz<sup>a,\*</sup>

<sup>a</sup>*Electrochemistry Laboratory, Paul Scherrer Institut, 5232 Villigen, Switzerland*

<sup>b</sup>*Institute of Materials, Ecole Polytechnique Federal de Lausanne, 1015 Lausanne, Switzerland*

<sup>c</sup>*Photon Science Division, Paul Scherrer Institut, 5232 Villigen, Switzerland*

<sup>d</sup>*ID16A - Nano-imaging beamline, The European Synchrotron Radiation Facility, 71 Avenue des Martyrs, Grenoble, 38043, France*

<sup>e</sup>*Univ. Grenoble Alpes, Univ. Savoie Mont Blanc, CNRS, Grenoble INP, LEPMI, 38000 Grenoble, France*

<sup>f</sup>*ESRF, The European Synchrotron, 71 Avenue des Martyrs, CS40220, 38043 Grenoble Cedex 9, France*

<sup>g</sup>*Laboratory of Physical Chemistry, ETH Zürich, 8093 Zürich, Switzerland*

\*Corresponding author, e-mail: [juan.herranz@psi.ch](mailto:juan.herranz@psi.ch)

## **ABSTRACT**

Non-noble metal catalysts (NNMCs) hold the potential to replace the expensive Pt-based materials currently used to speed up the oxygen reduction reaction (ORR) in proton exchange membrane fuel cell (PEMFC) cathodes, but they feature a poor durability that inhibits their implementation in commercial PEMFCs. This performance decay is commonly ascribed to the operative demetallation of their ORR-active sites, the electro-oxidation of the carbonaceous matrix that hosts these active centers and/or the chemical degradation of the ionomer, active sites and/or carbon support by radicals derived from the  $\text{H}_2\text{O}_2$  produced as an ORR by-product. However, little is known regarding the relative contributions of these mechanisms to the overall PEMFC performance loss. With this motivation, in this study we combined four degradation protocols entailing different cathode gas feeds (i.e., air vs.  $\text{N}_2$ ), potential hold values and durations to decouple the relative impact of the above deactivation mechanisms to the overall performance decay. Our results indicate that  $\text{H}_2\text{O}_2$ -related instability does not depend on the operative voltage, but only on the ORR charge. Moreover, the electro-oxidation of the carbon matrix at high potentials (which for the catalyst tested herein triggers at 0.7 V) seems to be more detrimental to the NNMCs' activity than the demetallation occurring at low potentials.

## INTRODUCTION

The strong reliance on the use of fossil fuels for transportation applications renders this sector one of the major contributors to the greenhouse gas emissions (accounting for  $\approx 24\%$  of the global anthropogenic  $\text{CO}_2$  inventory).<sup>1</sup> As a result, the extended adaptation of environmentally sustainable transportation technologies is crucial to achieve the stringent societal decarbonization targets required to mitigate climate change. Among these emerging technologies, proton exchange membrane fuel cells (PEMFCs) fueled with green  $\text{H}_2$  (i.e., produced using renewable energy sources<sup>2</sup>) are particularly appealing due to their fast refueling times, extended driving ranges and suitability for heavy-duty applications.<sup>3</sup> However, the market penetration of PEMFCs is still limited by their excessive cost, which is largely ascribed to the high Pt loadings (currently  $\geq 0.2 - 0.3 \text{ mg}_{\text{Pt}}\cdot\text{cm}^{-2}$ ) required to catalyze the oxygen reduction reaction (ORR) at their cathodes, and that is expected to account for  $\approx 40\%$  of the overall PEMFC stack cost once fuel cell electric vehicle (FCEV) manufacture volumes  $\geq 500,000$  FCEV per year shall be reached.<sup>4</sup> In order to tackle this issue, tremendous efforts are devoted to substitute these Pt-based materials with inexpensive non-noble metal catalysts (NNMCs). This has resulted in NNMC layers with initial low-current density performances similar to those of Pt-based catalyst layers (CLs), but featuring a PEMFC-durability that generally remains largely insufficient for their implementation in FCEVs.

Decades of research have led to a wide consensus linking this instability to operatively-induced changes in the species responsible for NNMC's ORR-activity, and that are in turn acknowledged to entail the involvement of one or more metal-based phases in the catalytic process (since metal-free catalysts generally feature a very low ORR-activity in acidic media).<sup>5</sup> In this regard, many experimental and computational studies have demonstrated that atomically-isolated metal (Me-) ions coordinated by 4 or more N-functionalities hosted in the catalyst's carbonaceous matrix (often referred to as  $\text{MeN}_x$  sites) possess an ORR-activity

whose intrinsic value (or turn-over frequency, TOF) is determined by fine differences in their coordination environment (e.g., number and nature of the direct coordination species, proximity of other surface groups and/or sites' location along the carbon matrix).<sup>6, 7</sup> Most NNMCs contain a multiplicity of these slightly different MeN<sub>x</sub> sites with disparate TOFs and intrinsic stabilities, along with Me-based particles (consisting of the reduced metal phase, oxides and/or carbides)<sup>8,9</sup> that are often encapsulated in a carbon shell and whose contributions to the catalyst's overall ORR-activity remains under debate.<sup>10</sup> Beyond this uncertainty, and in the specific context of the Fe-based NNMCs that generally feature the highest beginning-of-life device performance, the highly acidic reaction environment (pH  $\approx$  0) and relatively high potentials (typically  $>$  0.65 V vs the standard hydrogen electrode (SHE))<sup>11</sup> encountered by the catalysts in PEMFC cathodes are expected to cause the leaching of the iron in these particulate phases unless they are fully encapsulated in a protective carbon shell. For example, at room temperature, FeO(OH) is only foreseen to be thermodynamically stable at pHs  $\geq$  1.2 and potentials  $\geq$  0.77 V vs SHE.<sup>12-14</sup> By comparison, the thermodynamic stability of FeN<sub>x</sub> sites under PEMFC-cathode conditions remains under debate, with some density functional theory (DFT) studies endorsing that these sites are completely insensitive to dissolution<sup>15, 16</sup> and other computational<sup>16, 17</sup> and experimental<sup>7, 18</sup> works advocating for a much more restricted stability window. For instance, according to Holby *et al.*, at pH  $\approx$  0, FeN<sub>x</sub> sites would only be thermodynamically stable between  $\approx$  0.7 and  $\approx$  0.95 V vs. SHE.<sup>17</sup> In either case, the Fe cations leached from the FeN<sub>x</sub> sites and/or Fe-based particles could precipitate in the CL as Fe oxides seemingly stable under these condition<sup>7, 13, 19</sup> and/or attach to the sulfonic acid groups in the membrane and CL-ionomer, causing performance losses due to a poorer H<sup>+</sup>-conduction along these components.

The electro-oxidation of carbon is also known to play a crucial role in the stability of NNMC layers, particularly at high operative potentials. In this regard, carbon electro-oxidation

in Pt-based, carbon supported (Pt/C) catalyst is generally observed at potentials  $> 1.2$  V,<sup>20</sup> but NNMCs are often constituted by more disordered carbons on which this corrosion can take place at significantly lower potentials. As an example of this, Choi et al. observed CO<sub>2</sub>-release from an Fe-based NNMC already at potentials  $\geq 0.8$  V vs. the reversible hydrogen electrode (RHE) in 0.1 M HClO<sub>4</sub> electrolyte at 50 °C,<sup>13</sup> while other works reported significant carbon oxidation currents at cell voltages as low as 0.5 V.<sup>21, 22</sup> This electrochemical oxidation of the catalyst can be highly detrimental to its performance, since the subsequent destruction of the carbonaceous matrix hosting the FeN<sub>x</sub> sites and/or protecting the Fe-particles can trigger the demetallation issues discussed above.<sup>13, 23</sup> Moreover, the concomitant enrichment of the catalyst surface with oxidized carbon functional groups (e.g., phenols, carboxylic acids<sup>24</sup>) of hydrophilic character may be detrimental to the CL's water management / mass transport properties and worsen its high current density performance.<sup>22</sup>

Finally, the ORR on NNMCs reportedly leads to a significant amount of H<sub>2</sub>O<sub>2</sub> that is in turn known to decompose via Fenton reactions possibly triggered by the Fe-cations leaching from the catalyst upon PEMFC operation (*vide supra*), yielding highly aggressive radicals (e.g., ·OH, HOO·) that decompose the membrane and ionomer in the CL<sup>25</sup> as well as active sites, inducing again severe performance losses.<sup>12, 26</sup> As a result of this (and unlike in the case of Pt-based ORR-catalysts), the use of N<sub>2</sub> vs. O<sub>2</sub> (or air) as the cathode feed in NNMC-degradation protocols is known to lead to highly different results, since only the latter tests entailing cathodic O<sub>2</sub>-reduction also involve this H<sub>2</sub>O<sub>2</sub>-induced stability decay. More precisely, Choi et al. observed that exposing an NNMC to H<sub>2</sub>O<sub>2</sub> leads to an oxidation of the catalysts' carbonaceous matrix that lowers the TOF of its FeN<sub>x</sub> sites and consequently reduces its ORR-activity.<sup>26</sup> Complementarily, Kumar et al. recently reported that an electrochemical accelerated stress test (AST) in O<sub>2</sub>-containing electrolyte causes the loss of a significant fraction of the iron

in the NNMC's  $\text{FeN}_x$  sites due to the corrosion of the catalyst's carbon by  $\text{H}_2\text{O}_2$  and/or  $\text{H}_2\text{O}_2$ -derived radical species.<sup>27</sup>

The above-discussed multiplicity of NNMC-degradation pathways and their relation to the device's operative conditions (e.g., potential-dependent carbon electro-oxidation, ORR-related  $\text{H}_2\text{O}_2$ -production) implies that more than one of these mechanisms is likely to be at play upon PEMFC-operation. Despite this relevant aspect and the specificity of these mechanisms to NNMCs, these materials' durability is often assessed through ASTs that were originally designed to study the degradation of Pt-based catalysts,<sup>28</sup> which is preponderantly driven by the operative potential and independent of the presence / absence of  $\text{O}_2$  in the cathode gas feed.<sup>29</sup> Consequently, such ASTs generally entail extensive potential cycling using an inert gas (as opposed to air/ $\text{O}_2$ ) at the cathode, which for NNMCs would imply overlooking the plausible effects of ORR-byproducts on these catalyst's stability. While this important aspect has recently been addressed through revised, NNMC-specific protocols that implement  $\text{O}_2$ /air as the cathode reactant,<sup>30</sup> even such novel ASTs do not allow to differentiate the relative contributions of the above mechanisms to the overall PEMFC-performance losses. With this motivation, in this study we propose a novel approach for benchmarking NNMCs' durability through four degradation protocols in which the combination of different cathode gas feeds (i.e., air vs.  $\text{N}_2$ ), potential hold values and durations allow decoupling the relative contributions of the three deactivation paths discussed above to these materials' overall performance decay. We accomplished this by assessing the changes in the kinetic, ohmic and mass transport overpotentials inferred to an in-house synthesized NNMC by each protocol through a careful Tafel analysis and impedance spectroscopy measurements. Combining this with state-of-the-art imaging and analyses of the pristine and end-of-life CLs, our results reveal that carbon electro-oxidation is more detrimental to the catalyst's ORR-activity than Fe-demetalation, and suggest that  $\text{H}_2\text{O}_2$ -related instability only depends on the ORR charge transferred during the

protocol, and not on the applied potential. As such, we believe that this approach provides an excellent platform for the comparative benchmarking of NNMCs' operational durability.

## EXPERIMENTAL METHODS

**Catalyst Synthesis:** The catalyst used in this work was synthesized following the procedure provided for the 'wet BM-3mm' NNMC in our recent publications.<sup>31, 32</sup> In summary, polyacrylonitrile (PAN, Sigma-Aldrich), sodium carbonate ( $\text{Na}_2\text{CO}_3$ , Sigma-Aldrich, anhydrous, 99.999 % trace metal basis) and  $\text{Fe}^{2+}$  acetate (Sigma-Aldrich, > 99.99 % trace metal basis) pre-complexed with phenanthroline (Sigma-Aldrich, > 99 %) were used as the C-/N-precursor, pore inducing agent and Fe-precursor, respectively. Firstly, PAN and  $\text{Na}_2\text{CO}_3$  were stirred separately overnight in dimethylformamide (DMF, Sigma-Aldrich, anhydrous 99.8 % – in a  $\text{Na}_2\text{CO}_3$ /PAN:DMF weight ratio of 1:95) at 80 °C with a PAN to  $\text{Na}_2\text{CO}_3$  mass ratio of 1:2. After mixing and stirring these two solutions for an additional hour at 80 °C, the volume of an  $\text{Fe}^{2+}$ :phenanthroline complex solution (pre-prepared in DMF with a molar ratio of 1:5) needed for an Fe-content of 1 wt. % on the basis of all precursors' masses was added into the PAN and  $\text{Na}_2\text{CO}_3$  mixture. Afterwards, the solvent was evaporated until a viscous slurry was formed, and the latter was left overnight in a furnace at 80 °C to attain complete dryness. 1.5 g of the resulting dry precursor mixture underwent 16 h of wet-milling (planetary ball mill, Fritsch, Pulverisette, 45 mL  $\text{ZrO}_2$  crucible) in 10 mL of ethanol (VWR,  $\geq 99.8$  %, AnalaR NORMAPUR) with 3 mm diameter  $\text{ZrO}_2$  balls using a balls-to-precursor-mixture mass ratio of 27. The slurry obtained after wet-milling was passed through a 100  $\mu\text{m}$  sieve and dried. The resulting ground powder was then submitted to a first heat treatment (HT) in  $\text{N}_2$  (Messer AG, 5.0 – 200  $\text{mL}\cdot\text{min}^{-1}$ ) at 700 °C for 1 h. Afterwards, an acid treatment in 1 M sulfuric acid ( $\text{H}_2\text{SO}_4$ , Merck, 95-97 %) at 80 °C was performed for 4 h to remove soluble side-phases. After

water-rinsing and drying, this acid-washed powder underwent a second HT in 5 % H<sub>2</sub> (balanced with Ar, Pangas (5.0) – 200 mL·min<sup>-1</sup>) at 950 °C for 40 min.

**MEA preparation:** The membrane electrode assemblies (MEAs) were fabricated using a procedure similar to the one detailed in our previous publication.<sup>32</sup> Briefly, a commercial gas diffusion electrode (GDE – Johnson Matthey, 0.4 mg<sub>Pt</sub>·cm<sup>-2</sup> HISPEC 9100 Pt/HAS on a 1 × 1 cm<sup>2</sup> piece of Sigracet 25 BC gas diffusion layer (GDL)) used as the anode was hot pressed on a piece of Nafion<sup>®</sup> HP membrane (Ion Power) in order to obtain a half-MEA, as previously described in Ref. <sup>33</sup>. To prepare the cathode catalyst ink, a weighed amount of the above NNMC was dispersed in a mixture of isopropanol (Sigma-Aldrich, HPLC gradient grade, 99.9 %) and ultrapure water (18.2 MΩ·cm, ELGA Purelab Ultra) in a volume ratio of 3:7, yielding an ink with an NNMC-to-solvents ratio of 9 mg<sub>NNMC</sub>·mL<sub>H<sub>2</sub>O+IPA</sub><sup>-1</sup>, and with the volume of Nafion<sup>®</sup> ionomer solution (5 %, Sigma-Aldrich) required for an ionomer-to-catalyst mass ratio (ICR) of 0.6. After this ink was sonicated for 30 min, it was automatically sprayed (SONOTEK<sup>®</sup> ExactaCoat Automated Spray Coater) on the upper (i.e., cathode) side of the above half-MEA placed on a plate heated at 60 °C at a flow rate of 50 μL·s<sup>-1</sup> until achieving an NNMC cathode loading of ≈ 1 mg<sub>NNMC</sub>·cm<sup>-2</sup>. The precise loading of each cathode CL was determined by weighing the sample before and after spraying, and was systematically within the range of 1.2 - 1.4 mg<sub>NNMC</sub>·cm<sup>-2</sup> (leading to a CL thicknesses of 25-30 μm, as determined using a Mitutoyo MCD-25PX dial gauge with a nominal accuracy of ± 1 μm by measuring 5 different points on the MEA). Lastly, a carbon paper GDL (Sigracet SG29BC) was placed onto the NNMC layer prior to cell assembly. Freshly prepared MEAs were used for each degradation experiment.

**PEMFC tests:** The resulting assembly was placed inside a differential fuel cell with an active area of 1 cm<sup>2</sup> (of which the design was detailed in Ref. <sup>34</sup>) and compressed by selecting the total thickness of the gaskets resulting in a ≈ 25 % compression of the diffusion media in both anode and cathode sides (assuming that catalyst- and microporous-layers are incompressible).

All experiments were performed with a Bio-Logic VSP-300 potentiostat equipped with a 10 A / 5 V current booster. Prior to each degradation protocol, the initial ORR-activity of the cathode CL was assessed by recording a polarization curve galvanostatically (i.e., holding the current at selected values for 90 s) starting from the open circuit voltage (OCV) and down to a current value corresponding to a voltage slightly above  $\approx 0.7$  V; this relatively high cutoff potential was selected in order to minimize the deactivation of the CL in this verification of the initial performance and prior to the actual degradation experiment. After each degradation protocol, however, a full polarization curve between the OCV and  $0.8 \text{ A}\cdot\text{cm}^{-2}$  was recorded in a similar way as described above. Note that the potentials reported on the polarization curves correspond to the average values during the last 30 seconds of each current hold. Following each measurement at a given current, the corresponding high frequency resistance (HFR) was obtained by galvanostatic electrochemical impedance spectroscopy (GEIS) with a 10 % current perturbation in a frequency range of 1 MHz to 500 mHz and with 6 points per decade. All polarization curves were recorded at  $80 \text{ }^\circ\text{C}$ ,  $1.5 \text{ bar}_{\text{abs}}$  and 100 % relative humidity (RH) using  $600 \text{ mL}\cdot\text{min}^{-1}$  of  $\text{H}_2$  (Pangas 5.0) and  $1000 \text{ mL}\cdot\text{min}^{-1}$  of air (Messer AG, 5.5) at anode vs. cathode, respectively. Following the recording of this end-of-life, full polarization curves, potentiostatic electrochemical impedance spectroscopy (PEIS) tests at  $0.2 \text{ V}$  (with a  $5 \text{ mV}$  perturbation) were performed with the PEMFC still at  $80 \text{ }^\circ\text{C}$  and  $1.5 \text{ bar}_{\text{abs}}$  but with fully humidified  $\text{H}_2$  and  $\text{N}_2$  feeds at the anode and cathode, respectively, in order to determine the  $\text{H}^+$  conduction resistance in the NNMC layers ( $R_{\text{H}^+, \text{cathode}}$ ).<sup>35</sup> The resulting spectra were fitted to the transmission line model (TLM, with  $X^2 < 0.005$ ) using the Z-fit package included in the EC-Lab<sup>®</sup> V11.36 software. Lastly, the cell was cooled down to room temperature and cyclic voltammograms (CVs) were recorded between  $0.05$  and  $1.00 \text{ V}$  with a scan rate of  $50 \text{ mV}\cdot\text{s}^{-1}$  at ambient pressure, with a  $\text{H}_2$  flow rate of  $100 \text{ mL}\cdot\text{min}^{-1}$  at the anode and the  $\text{N}_2$  flow at the cathode stopped. As a control sample, one full polarization curve of an additional MEA

prepared from the pristine NNMC was also recorded without applying any degradation protocol, but including the PEIS and CV measurements in the similar conditions applied for the degraded samples described above. The ORR-activities ( $i_{kinS}$ ) before and after each degradation protocol were obtained from the linear regime of the corresponding Tafel plots at 0.8 V. Carbon electro-oxidation experiments were performed by repeating the protocol followed for the recording of the polarization curves (i.e., holding the potentials at selected values for 90 s) between OCV and 0.45 V, using the same conditions in which the H<sub>2</sub>/Air polarization curves were recorded but replacing the cathode feed with N<sub>2</sub>. As above, the reported currents correspond the average values during the last 30 seconds of each potential hold.

**Determination of the mass transport overpotential ( $\eta_{tx}$ ):** In order to quantify the mass transport overpotential ( $\eta_{tx}$ ) at the beginning- and end-of-life (i.e., before and after each degradation protocol), the overall cell potential ( $E_{cell}$ ) was decoupled based on Equation 1,<sup>36</sup> which relies on the assumption that the kinetic and H<sup>+</sup>-conduction overpotentials for the hydrogen oxidation reaction at the PEMFC's anode CL are negligible.<sup>37</sup>

$$E_{cell} = E_{rev} - i \cdot R_{HFR} - i \cdot R_{H^+,cathode}^{eff} - \eta_{ORR} - \eta_{tx} \quad (1)$$

where  $E_{rev}$  is the thermodynamic equilibrium potential (in turn a function of the gases' partial pressures and PEMFC temperature),<sup>38</sup>  $R_{HFR}$  corresponds to the sum of membrane H<sup>+</sup>-conduction resistance and contact and bulk electronic resistance that can be determined by the high frequency resistance (HFR) in impedance measurements,  $i$  is the applied current density,  $R_{H^+,cathode}^{eff}$  is the effective H<sup>+</sup>-conduction resistance of the cathode CL,  $\eta_{ORR}$  is the cathodic ORR-overpotential, and  $\eta_{tx}$  is the mass transport overpotential caused by O<sub>2</sub> concentration gradients in the electrode due to gas transport resistances.

After determining  $R_{H^+,cathode}$  in the CLs from the fits of the impedance spectra recorded in  $H_2/N_2$  by applying the TLM, the effective  $H^+$ -conduction resistance ( $R_{H^+,cathode}^{eff}$ ) in the CL was calculated using the Equation:

$$R_{H^+,cathode}^{eff} = \frac{R_{H^+,cathode}}{3+\zeta} \quad (2)$$

where  $\zeta$  is a dimensionless correction factor that depends on the product of current density and the  $H^+$ -conduction resistance divided by the intrinsic Tafel slope if the ORR ( $b$ ), (i.e., on  $(i \cdot R_{H^+,cathode})/b$ ), and that can be read out in Figure 2 of Ref. <sup>36</sup> For the ORR on NNMCs used in this study, a Tafel slope of  $70 \text{ mV} \cdot \text{dec}^{-1}$  (at  $80 \text{ }^\circ\text{C}$ ) was considered for this analysis. The polarization curves corrected for the  $R_{HFR}$  and  $R_{H^+,cathode}^{eff}$  terms over the entire current density range after each degradation protocol (provided in Figure S10) were used to estimate the  $\eta_{tx}$  values by quantifying the difference in potential between the extrapolated Tafel lines and the polarization curves corrected for these ohmic losses (i.e.,  $R_{HFR}$  and  $R_{H^+,cathode}^{eff}$ )

**Sample preparation for scanning transmission electron microscopy (STEM) and X-ray fluorescence (XRF) analyses:** STEM/EDS measurements of the Fe-based nanoparticles' composition were performed on catalyst particles scrapped from the NNMC MEAs and dispersed in 1:4 DI water:isopropanol in an ultrasonic bath. 2-4  $\mu\text{L}$  of this ink was placed on ultrathin lacey carbon TEM copper gris (Electron Microscopy Science) and allowed to dry. The spatially resolved XRF and STEM measurements were performed on pristine and *post mortem* MEAs that were embedded in EPON<sup>TM</sup> epoxy resin in a two-step process, first in a 1:1 acetone:EPON mixture and subsequently in pure EPON. For 2D mapping, 150 nm thick slices were prepared using a microtome setup confirmed via optical inspection. Sections for STEM analysis were transferred on ultrathin lacey carbon TEM copper grids and for XRF on 500 nm thick graphene coated silicon nitrate membranes. For 3D XRF computed tomography (-CT),

mm-sized pieces of the embedded CL were glued onto individual custom-built tomography pins using a pre-cured epoxy to avoid sample contamination.<sup>39</sup> These pins were mounted on a custom-built micro-lath and a cylinder was milled out with a diameter of  $\approx 70 \mu\text{m}$  and a height of  $100 \mu\text{m}$ .<sup>40</sup> The diameter of the pre-milled samples was further reduced to  $36 \mu\text{m}$  for the pristine sample and to  $42 \mu\text{m}$  for the ‘Air-0.5 V’ sample using a Xenon plasma Focussed Ion Beam (FIB). In all preparation steps, the samples were handled with utmost care to avoid any type of contamination and to allow the quantitative analysis of the XRF measurements.

**STEM analysis:** energy dispersive X-ray spectroscopy (EDS) mapping and high-angle annular dark field (HAADF) imaging were performed on a ThermoFischer Scientific Orisis TEM equipped with four windowless X-ray detectors with a  $0.9 \text{ srad}$  solid angle and operated in scanning mode at  $200 \text{ kV}$  and at room temperature. A probe current of  $1 \text{ nA}$  was used and EDS acquisitions were performed with a dwell time of  $100 \mu\text{s}$ , integrating  $512 \times 512 \text{ px}$  frames over 10 cycles. The pixel size of these acquisitions was  $27.7 \text{ nm}$  for the microtomed samples and  $0.65 \text{ nm}$  for the dispersed ones. The Velox software was used for EDS analysis. All lines and spectra were fitted and deconvoluted and weight fractions were computed using the standardless k-factor method. To cover the entire CL thickness, image stitching was performed with an in-house code written in python and using the sci-kit image library. To study the Fe-rich secondary phases,  $> 10$  HAADF images with a  $1.2 \text{ nm}$  pixel size were acquired from the cross-sections of each investigated sample. The bright Fe precipitates were segmented with a pixel classifier implemented in the Ilastik software.<sup>41</sup> All intensity, edge and texture features were selected with sigma 1, 3, and 10. A morphological open operation was performed on the resulting binary maps to separate particles in contact. Each particle was then identified with a labeling operation and measurements of their maximum Feret diameter, aspect ratio, projected area and number of particles per image were performed using FIJI’s MorpholibJ plugin<sup>42</sup> and the python sci-kit image library.

**Nano-XRF imaging:** 2D X-ray fluorescence (XRF) mapping and 3D XRF computer tomography (XRF-CT) were performed at the ID16A-NI beamline of the European Synchrotron Radiation Facility (ESRF). The experiments were performed at 17 keV with the X-ray beam focused by two multilayer-coated Kirkpatrick-Baez (KB) mirrors. The mirrors focused the beam down to a 68 nm (h) by 37 nm (v) spot size. The incident flux used was  $4 \times 10^{11}$  photons/s. The XRF data was acquired in scanning mode with a 20 nm step size for 2D mapping and a 200 nm step size for the CT measurements. The X-ray fluorescence signal was captured by two detectors mounted at  $90^\circ$  with respect to the incoming beam on two opposing sides of the sample. Both detectors and the sample were mounted in a vacuum chamber to minimize air absorption and scattering. Furthermore, the detectors were calibrated using an AXO X-ray fluorescence calibration target. The weighted signal from the two calibrated detectors allows a quantitative measurement of iron (Fe  $K\alpha$ , at 6.4 keV) and sulfur (S  $K\alpha$ , 2.31 keV). The acquired spectra were fitted with PyMca software. For the XRF-CT, 100 projections were recorded for both the pristine and 'Air-0.5V' samples (*vide infra*). After the alignment of the projections, tomographic reconstructions of the Fe  $K\alpha$  line were performed with an iterative maximum likelihood estimation method (MLEM)<sup>43</sup> algorithm using 100 iterations. Image analysis of tomographic slices was performed with the Matlab Image Processing Toolbox and 3D renderings were created using the Avizo software package 2021.

**X-ray diffraction (XRD):** The XRD measurement was performed on a SmartLab Rigaku system. The measurement was carried out for  $2\theta$  angles between  $5^\circ$  and  $90^\circ$  using a copper rotating anode (Cu  $K\alpha = 1.5406 \text{ \AA}$ ), a Cu  $K\beta$  filter, and a Rigaku HyPix3000 detector. All measurements were performed in the Bragg–Brentano mode with the Cu-source set to 160 mA and 40 kV.

**X-ray absorption spectroscopy (XAS):** *Ex situ* XAS measurements were carried out at the SuperXAS (X10DA) beamline of the Swiss Light Source (SLS). The spectra were recorded

for 4 minutes using quickXAS<sup>44</sup> at the Fe K-edge (7.112 keV) in transmission mode. Each sample was prepared by filling the catalyst powder into a Kapton capillary that was placed between two ionization chambers (15 cm long) filled with 1 bar of N<sub>2</sub> to measure both the incident and transmitted beam intensity. The polychromatic beam from the 2.9 T bending magnet (the SLS operated at 400 mA and 2.4 GeV) was collimated by a Si-coated collimating mirror at 2.9 mrad, subsequently monochromatized by a liquid nitrogen-cooled Si(111) channel-cut monochromator oscillating at 1 Hz, and focused using a Rh-coated toroidal double-focusing mirror giving a spot size of 1 mm × 0.2 mm. An Fe-foil was placed before a third ionization chamber measured in parallel and its spectrum was subsequently used as a reference for energy calibration by aligning the maximum of the first derivative of the reference spectrum to 7.112 keV ( $E_0$ ) for all sample spectra. The data treatment and analysis including calibration, background correction, normalization and linear combination fitting (LCF) was carried out using both the ProQEXAFS<sup>45</sup> and the Demeter<sup>46</sup> software packages, and the LCFs were carried out between  $E_0 - 50$  eV (7.062 keV) and  $E_0 + 110$  eV (7.222 keV) with the fit forced to sum up to unity.

**Raman Spectroscopy:** The Raman spectra were recorded on a Renishaw inVia Raman system, with an excitation wavelength at 532 nm. Measurements were performed in a backscattering configuration, using a 50x objective (NA = 0.85), and a 2400 grooves mm<sup>-1</sup> grating. This configuration ensured a spectral resolution much better than 1 cm<sup>-1</sup>. To decrease the power density at the sample, the line mode of the spectrometer was used. This configuration allowed to record ‘averaged’ spectra over an area of *ca.* 50 μm<sup>2</sup> in a single shot, with a power density at the sample much less than ~ 50 μW μm<sup>-2</sup>. These conditions effectively ensured that the sample was not degraded/modified during the analysis. For visualization purposes, the spectra were simply normalized to the amplitude of the so-called ‘G’ mode that peaks at ~ 1600 cm<sup>-1</sup>, after subtracting the background signal.

## RESULTS and DISCUSSIONS

The NNMC used in this work was prepared using the same approach presented in our previous publication (abbreviated as ‘wet-BM-3mm’ in Ref. <sup>32</sup>), and the results of its detailed characterization are available in the same work.<sup>32</sup> In brief, this Fe-based catalyst possesses a surface area of  $\approx 1000 \text{ m}^2\cdot\text{g}^{-1}$ , and its visual inspection unveils that it contains Fe-based nanoparticles (NPs) preponderantly encapsulated in carbon shells (see Figure S1). Our previous characterization by Mössbauer spectroscopy of a similarly-prepared set of catalysts unveiled that these NPs consist of a small fraction of  $\text{Fe}^0$  and a majority of  $\text{Fe}_3\text{C}$ ,<sup>9</sup> of which the presence in the current NNMC is corroborated by the X-ray diffractogram featured in Figure S2. Moreover, in the same study<sup>9</sup> the multivariate curve resolution analysis of the NNMCs’ X-ray absorption near edge structure (XANES) spectra allowed to isolate the spectral components of their  $\text{FeN}_x$  sites and NP-based side phases. When those same component spectra were used to fit the XANES of the NNMC featured herein, they yielded an excellent fit (cf. Figure S3) from which we inferred that  $\approx 25$  vs.  $\approx 75$  % of the sample’s total atomic metal inventory (1.8 wt. % Fe) is featured in the form of  $\text{FeN}_x$  sites vs. Fe-based NPs, respectively. Based on our experience with similarly-prepared NNMCs, their ORR-activity linearly increases with their content of  $\text{FeN}_x$ -sites, but catalysts featuring  $\approx 90$  % of their metal inventory in the form of Fe-nanophases still display a non-negligible catalytic performance.<sup>9, 47</sup> Thus, the ORR-activity of the NNMC in this work may not exclusively stem from its  $\text{FeN}_x$ -sites, but also from C-encapsulated Fe-nanoparticles and/or surface N-functionalities hosted in their carbon shells that have been shown to possess a non-negligible ORR-activity.<sup>10, 48</sup>

In order to decouple the contribution of the different degradation mechanisms to this catalyst’ PEMFC performance decay, we designed four protocols at two different potentials of 0.5 or 0.8 V and using either air or  $\text{N}_2$  as the cathode gas feed. The detailed conditions of these

protocols and the corresponding degradation pathways expected to be at play in each of them are visually summarized in Figure 1. Note that each protocol was performed using a freshly prepared NNMC layer of which the initial ORR-activity was verified at the beginning of each protocol by recording a polarization curve from the OCV down to a maximum potential of  $\approx 0.7$  V.

Looking at the details behind each protocol, the one denoted as ‘Air-0.5V’ consists of a 1 h potential hold at 0.5 V with air fed to the cathode, and thus involves operative conditions under which Fe-demetalation as well as H<sub>2</sub>O<sub>2</sub>-induced effects can be expected to affect the performance of the NNMC layer. In order to isolate the effect of the former mechanism (i.e., Fe-demetalation) under equivalent condition, the ‘N<sub>2</sub>-0.5V’ protocol entails the same potential hold value and duration, but eliminates the occurrence of H<sub>2</sub>O<sub>2</sub>-related effects by using N<sub>2</sub> instead of air as the cathode feed. Next, the ‘Air-0.8V’ protocol was designed to study the performance decay at a higher potential of 0.8 V in which a significantly lesser extent of Fe-demetalation is expected,<sup>13, 14</sup> but carbon electro-oxidation may appear along with the H<sub>2</sub>O<sub>2</sub>-effects intrinsic to the use of air in the cathode feed. Chiefly, the duration of the ‘Air-0.8V’ test was adjusted to match the ORR-charge that had been previously observed in the one-hour-long, ‘Air-0.5V test’; due to the significantly lower current recorded at this higher potential, this translated in a hold duration of  $\approx 250$  h (see Figure S4 for the time dependent currents recorded in each protocol). Finally, the ‘N<sub>2</sub>-0.8V’ protocol is identical to the previous one but is performed with N<sub>2</sub> as opposed to air as the cathode feed, and therefore serves to isolate the exclusive effect of carbon electro-oxidation on the catalyst’ performance decay (and, possibly, metal-dissolution)<sup>13, 14</sup> at this potential.

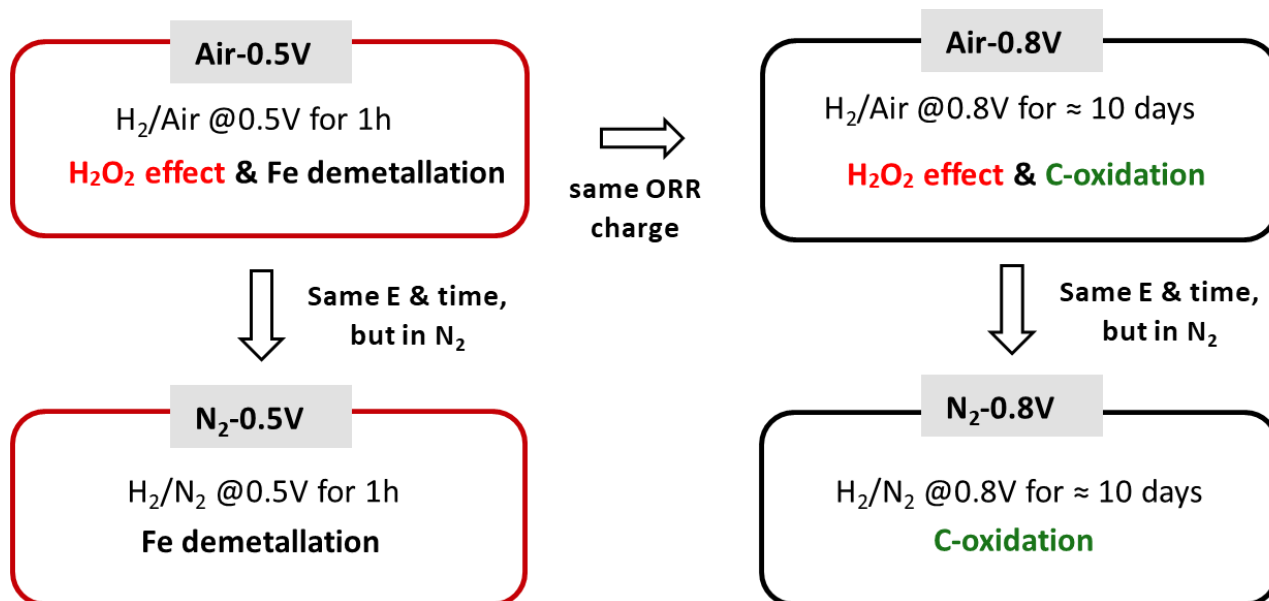


**Figure 1.** Schematic representation of the various stability protocols used in this study, along with the degradation pathways expected to be at play in each protocol.

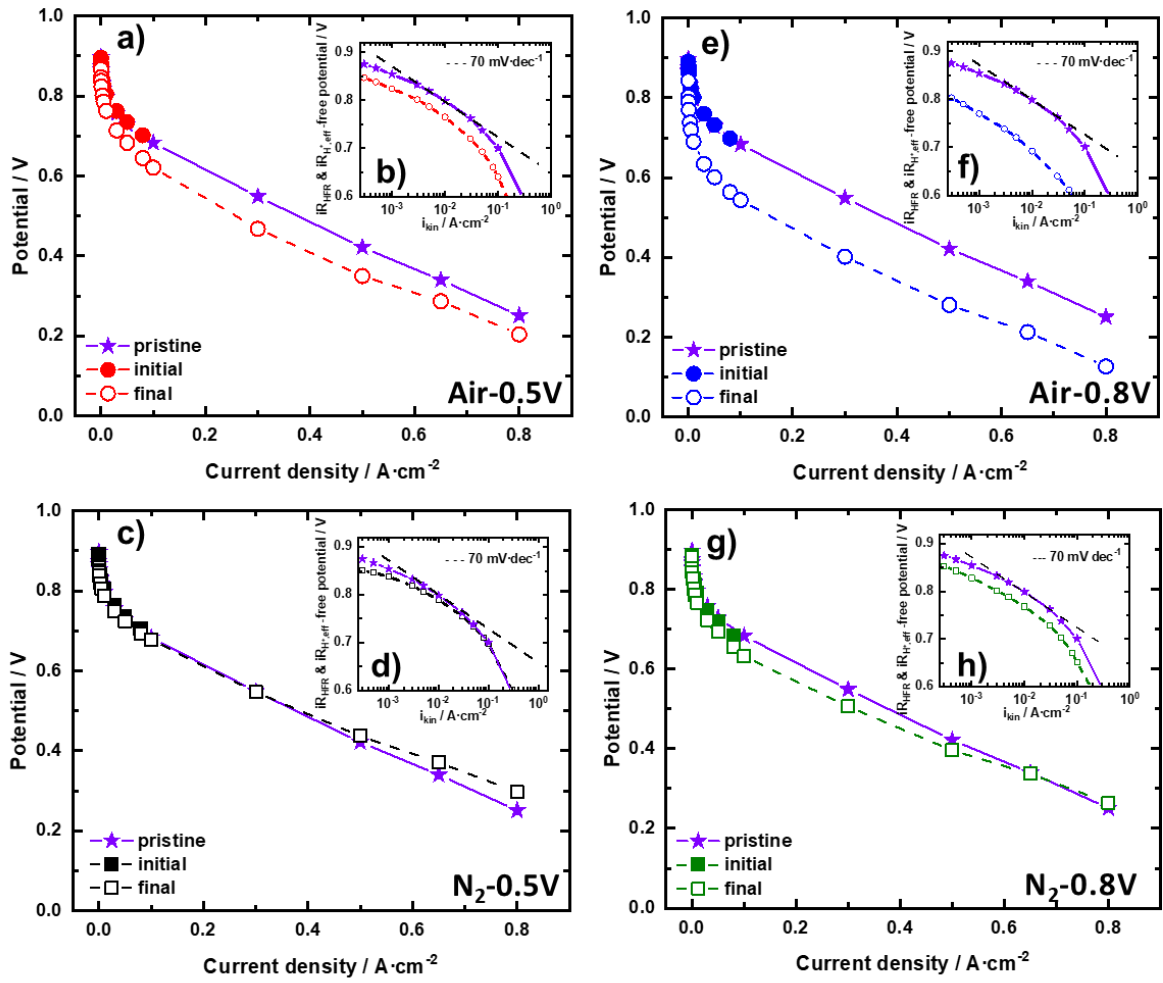


**Figure 2.** PEMFC H<sub>2</sub>/Air polarization curves recorded at 1.5 bar<sub>abs</sub>, 80 °C and 100% relative humidity with a cathode loading of 1 mg<sub>NNMC</sub>·cm<sup>-2</sup> (a, c, e, g) before and after the degradation protocols in Figure 1, along with their corresponding Tafel plots corrected for HFR and H<sup>+</sup>-conduction resistance related losses (b, d, f, h).

We started investigating the NNMC's performance decay in the protocols performed at 0.5 V and using air vs. N<sub>2</sub> as the cathode feeds (i.e., 'Air-0.5V' vs. 'N<sub>2</sub>-0.5V', respectively), for which the corresponding polarization curves and Tafel plots are displayed in Figure 2a-d. The mass-normalized ORR-activities at 0.8 V at the beginning-of-life ( $\approx 8 \text{ A}\cdot\text{g}_{\text{NNMC}}^{-1}$  at 80 °C and an O<sub>2</sub>-partial pressure ( $p_{\text{O}_2}$ ) of 0.21 bar, corresponding to  $\approx 27 \text{ A}\cdot\text{g}_{\text{NNMC}}^{-1}$  at  $p_{\text{O}_2} = 1 \text{ bar}$ )<sup>32</sup> and at the end of each protocol are also summarized in Figure S5, and the corresponding

activity losses normalized with regards to the beginning-of-life value are featured in Figure 3. The latter unveils that, after the ‘Air 0.5V’ protocol, the kinetic performance decreased by  $\approx 70\%$  of its initial value, and this was accompanied by a significant drop of the high current density performance that is further discussed below (Figure 2a,b). By comparison, when the same protocol was performed in the absence of  $O_2$  at the cathode (i.e., in ‘ $N_2$ -0.5V’), the mass-normalized ORR-activity only decreased by  $\approx 30\%$ , and the potential at the highest measured current of  $0.8\text{ mA}\cdot\text{cm}^{-2}$  even increased slightly (Figure 2c,d). Notably, the non-negligible ORR-activity decrease observed even in the ‘ $N_2$ -0.5V test’ suggests that the relatively low potential of  $0.5\text{ V}$  in this protocol leads to a certain extent of demetallation from the Fe-based nanoparticles’ and/or  $FeN_x$  sites’ responsible for this catalyst’s ORR-activity, and/or to a decrease of their TOF.<sup>10, 18</sup>

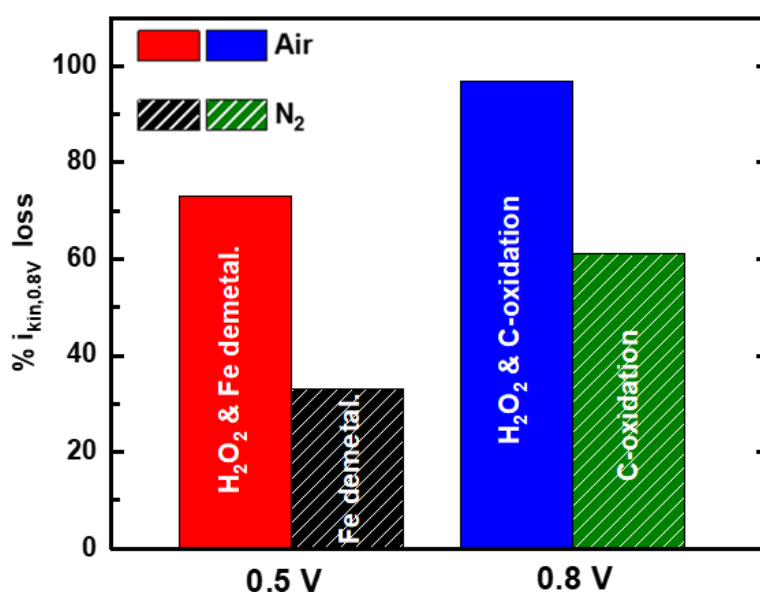


**Figure 3.** Summary of the losses in mass-normalized ORR-activity at  $0.8\text{ V}$  (expressed as a percentage with respect to the beginning-of-life value) inferred by each of the stability protocols.

To evaluate Fe-demetalation and H<sub>2</sub>O<sub>2</sub>-related degradation effects during the ‘Air-0.5 V’ protocol in terms of morphology and elemental composition of the NNMC layer, we investigated a pristine CL and the post-mortem, end-of-life sample with STEM and XRF microanalysis. Figure 4a (top) shows a cross-section of a catalyst layer and indicates a typical region that was analysed with STEM-EDS and HAADF to access the spatial Fe-distribution in the CLs. Elemental mapping of the weight fraction of Fe acquired across the thickness of the end-of-life CL (shown in Figure 4b) indicates the presence of Fe-rich clusters in the NNMC layer after the ‘Air-0.5V’ degradation protocol. The corresponding HAADF image unveils that these clusters correlate with high-brightness NPs that are observed at higher resolution in Figure S1 and S6a-b, and are typically embedded in thick, semi-graphitized carbon shells. A comparison with the pristine samples reveals that the spatial distribution of Fe clusters is qualitatively similar in the pristine and ‘Air-0.5V’ CLs (see the maps in Figure S6d-e). This is further confirmed by measurements of the average Fe weight fraction in six 100<sup>2</sup> μm<sup>2</sup> areas of each sample (Figure S6j), where no significant changes or trend was detected with the error bars from standard deviation largely overlapping for the pristine and post-mortem CLs. We note, however, that the weight fractions were computed using a standardless method (namely, the k-factors, see Methods) which is semi-quantitative in nature.

Changes in the Fe-rich agglomerates were then investigated with respect to their morphology in the pristine and post-mortem CLs using HAADF-STEM images (displayed in Figure S7a-b) of a total area of 60-70 μm<sup>2</sup> with a resolution allowing to resolve single particles down to a 5-10 nm size. The complete results inferred from these measurements are presented in Table S1. Within the accumulated statistics (> 730 particles for each sample), no significant decrease in the number of particles per image (Figure 4c) nor changes in the distribution of their size (Figure 4d) or aspect ratio (major over minor diameter of a fitted ellipse, Table S1) as a result of the degradation protocol could be detected. Thus, the electron microscopy and

spectroscopy results seem to indicate that most Fe-particles have withstood the ‘Air-0.5V’ degradation test, which is not surprising considering that the majority of them appear to be fully protected by thick carbon shells (cf. Figure S1). An alternative explanation is that the “Air-0.5” protocol caused leaching of the Fe cations from the catalyst that precipitated along the CL in the form of Fe-based NPs (under these conditions, expected to be Fe-oxides) with a shape and size similar to that of the carbon-encapsulated agglomerates present in the pristine catalyst – a possibility that cannot be ruled out, but that appears highly unlikely based on the good agreement among beginning- and end-of-life results and on the large statistics intrinsic to these measurements. This is endorsed by the fact that, in our microscopic examination of multiple locations along the *post mortem* CL, we did not find any metallic nanoparticles devoid of a protecting carbon shell (as one would have expected from the non-encapsulated Fe-oxides reported to form during potential-cycling ASTs).<sup>27</sup> Finally, the analysis by EDS of these end-of-test particles strongly suggests that they preponderantly consist of the non-oxidic, Fe<sub>3</sub>C-phase featured in the pristine catalyst (see Fig. S8).

Complementarily to this, we carried out a synchrotron-based high-resolution x-ray fluorescence (XRF) nano imaging study in order to quantify more precisely the total Fe contents in the same pristine and post-mortem, ‘Air-0.5V’ samples. These experiments were conducted at a dedicated instrument of the ID16A-NI beamline at the European Synchrotron Radiation Facility (ESRF), operating in vacuum and cryogenic conditions that facilitate quantitative measurements of the atomic distribution of Fe with a sensitivity down to few tens of atoms. 2D XRF mapping at 20 nm resolution of the pristine and post mortem samples after ‘Air-0.5V’ was conducted are shown in Figure S9, and unveil that the recorded images look fairly similar to those of the STEM-EDS study. However, XRF’s enhanced sensitivity provides additional and quantitative information on the CLs’ Fe-content, and thus a comparison of different positions from the microtomed CLs unveils a  $\approx 15\%$  decrease in the Fe-content of

the end-of-life sample compared to the pristine one. This apparent decrease is limited to a statistically small volume of 30-40  $\mu\text{m}^3$ , so additional 3D XRF-CT measurements were performed to overcome these limitations with a beamsize of 200 nm that translates into probed volumes of  $\approx 6000 \mu\text{m}^3$  for both CLs. The tomographic reconstructions in Figure 4e represents the 3D rendering of the Fe distribution (based on the Fe  $K\alpha$  line, and for a representative sub-volume of  $6 \times 30 \times 30 \mu\text{m}^3$ ) using a color scale that allows identifying subtle changes in the content and distribution of Fe atoms. In case of the pristine sample, a subtle shift of intensity towards higher Fe-contents is represented by the yellow color within the CL. These changes are evenly distributed across the sample, indicating that this pristine CL has a higher content of Fe-atoms per voxel compared to the almost uniformly colored post-mortem sample. While the 3D rendering visualizes the spatial distribution, a histogram representing the average Fe content can better evidence the potential leaching of Fe. Thus, we carried out a simple segmentation protocol based on gradient and signal strength to mask out air voxels and extract the Fe-content in units of atoms per  $200 \text{ nm}^3$  voxels. The results of this approach are shown as a histogram in Figure 4f, in which the pristine sample exhibits a broader peak centered at  $\approx 220$  Fe-atoms while the post-mortem CL features a sharper distribution centered at  $\approx 140$  Fe-atoms. We then integrated the intensity of all voxels within the CL to assess the average number of Fe atoms per voxel in both layers, and found an overall loss of  $\approx 18 \%$  of the Fe atoms (with regards to the pristine CL's content, and depicted in the inset of the histogram) that agrees very well with the results of the 2D nano-XRF analysis. We note in passing that the  $\approx 15\text{-}20 \%$  lower Fe-content in the post mortem sample is not related to differences between the catalysts loadings of the pristine and 'Air-0.5V' CLs used for these analysis, since their loadings were 1.3 vs.  $1.4 \text{ mg}_{\text{NNMC}} \cdot \text{cm}^{-2}$ , respectively.

If one combines this confirmation of Fe-dissolution with the shift in the Fe distribution towards smaller sizes inferred from the histograms, Fe-leaching in the course of this 'Air-0.5V'

protocol must occur mainly from within voxels with fewer metal atoms. Indeed, Fe precipitates with a size around 20-50 nm like the ones imaged by HAADF would consist of at least a couple of thousand Fe atoms within one voxel (assuming a ferrite body-centered cubic crystal structure and sizes as those seen by HAADF). Importantly, from integrating the total Fe content of voxels with intensities  $> 1000$  atoms, no significant differences between the pristine and post-mortem sample after the 'Air-0.5V' protocol are inferred. In other words, the absence of significant changes in the Fe contents of the pristine and end-of-life samples within the range of high intensity voxels assignable to Fe-based nanoparticles implies that these side-phases did not undergo any demetallation (in agreement with what was qualitatively inferred from the HAADF images), and indirectly suggests that the loss of Fe deduced from the histograms' integration likely stems from the partial demetallation of the atomically dispersed FeN<sub>x</sub> sites in this NNMC.

Beyond its specific origin, the confirmation that Fe dissolves upon PEMFC operation at 0.5 V may imply the presence within the CL of Fe-cations that could aid the decomposition of ORR-produced H<sub>2</sub>O<sub>2</sub> into aggressive radicals that would in turn chemically degrade the membrane and ionomer. On top of this, such cationic species could additionally place-exchange with the protons in the ionomer and membrane's sulfonic acid groups, effectively decreasing their H<sup>+</sup>-conduction capabilities. Either of these effects should therefore be detectable in the impedance spectra of the post-mortem sample, which essentially featured the same R<sub>HFR</sub> as the pristine CL and a  $\approx 10\%$  higher R<sub>H<sup>+</sup>, eff</sub> value (see Figures S10 and S11 for the impedance spectra and corresponding R<sub>HFR</sub> and R<sub>H<sup>+</sup>, eff</sub> values derived from their fits, respectively). These minor changes in the impedance results indicate that the operative release of Fe did not result in noticeable H<sub>2</sub>O<sub>2</sub>-related degradation of the membrane and/or the ionomer, at least within the rather short time scale (1 h) of this 'Air-0.5V' protocol. Notably, the lack of ionomer degradation was also confirmed by the F-EDS cross-section images of the

CLs acquired by STEM, where there was no clear difference in fluorine distribution between the pristine CL and the sample submitted to the ‘Air-0.5V’ protocol (Figure S6g, h). On the other hand, the slight increase in  $R_{H^+, \text{eff}}$  observed for the *post mortem* CL may be partially caused by the poisoning of the ionomer’s sulfonate groups with leached Fe-ions. More precisely, based on the CL’s NNMC-loading ( $1 \text{ mg}\cdot\text{cm}^{-2}$ ) and ICR (0.7), along with the ionomer’s equivalent weight ( $1100 \text{ g/molSO}_3^-$ ), the  $\approx 10 \%$  higher  $R_{H^+, \text{eff}}$  value would result from the release of  $\approx 6 \%$  of the CL’s iron content as  $\text{Fe}^{3+}$  (assuming that each of these ferric ions poisons three sulfonate groups). Notably, this would correspond to leached iron that would be trapped within the CL, implying that the total amount of dissolved Fe would be larger than the  $\approx 15 \%$  decrease of the metal inventory estimated by the above XRF measurements (which would correspond to Fe-ions leaving the cell).

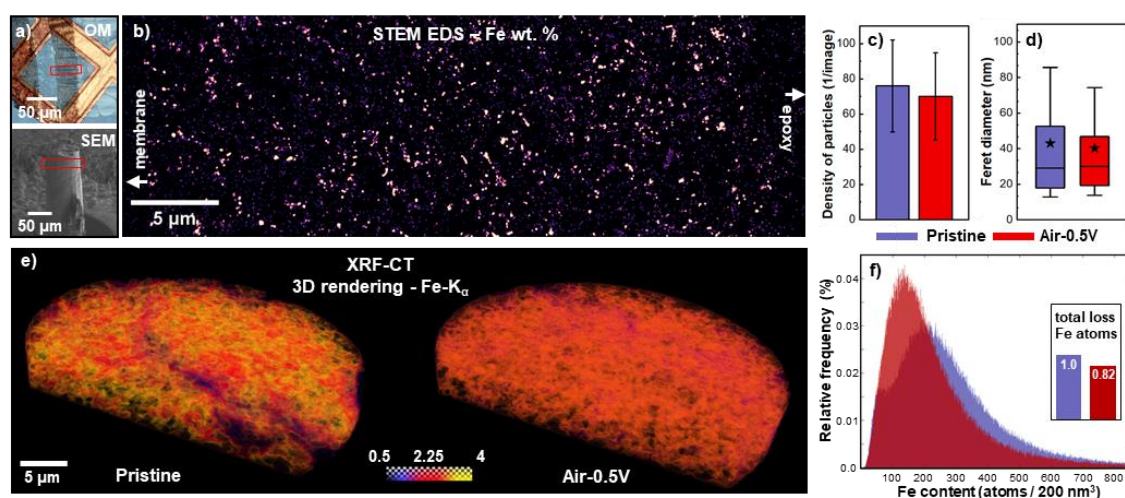


**Figure 4.** STEM and XRF analysis of pristine vs. end-of-life samples before and after the ‘Air-0.5V’ stability test. Overview images of the samples prepared for STEM and XRF measurements (a), consisting of a light microcopy image of an embedded and microtomed section of the MEA prepared for STEM imaging on a copper grid (top) and an SEM image of the  $40 \mu\text{m}$  pillar used for 3D XRF-CT measurements (bottom), whereby the red frames indicate representative regions of interest for each measurements. STEM-EDS map of the relative counts of the Fe  $K\alpha$  line in a microtomed cross-section of the end-of-life CL (b) and comparison

of the number of Fe precipitates per  $2.5 \times 2.5 \mu\text{m}^2$  image and of the distribution of the particle size inferred from their Feret diameter for the pristine or end-of-life CLs (purple vs. red, respectively) (d). Note that the error bars in (c) correspond to one standard deviation, whereas in (d) the boxes correspond to 1<sup>st</sup>, 2<sup>nd</sup> and 3<sup>rd</sup> quartiles, the whiskers represent outliers (1.5x interquartile range) and the stars stand for the mean values. 3D rendering of the Fe K $\alpha$  line for the pristine and end-of-life CLs based on tomographic reconstructions of the XRF-CT measurements (with a voxel size of  $200 \text{ nm}^3$ ), with the pristine and end-of-life layers on the left vs. right of the image, respectively (e). Note that the color scale is limited between 0 and  $4 \text{ ng}\cdot\text{mm}^{-2}$ . Fe distributions within the pristine and end-of-life CLs inferred from 3D XRF-CT, with the inset depicting the total loss of Fe atoms throughout the complete volume of  $6000 \mu\text{m}^3$  (f).

Following this investigation of the processes in the degradation tests at 0.5 V, we now assess the performance changes in the protocols performed at a higher potential of 0.8 V that, as discussed above, is likely to entail the electrochemical corrosion of the catalyst's carbonaceous matrix. Since the onset potential of this reaction is expected to strongly depend on the graphitization degree of the NNMC type,<sup>21, 22</sup> we performed a preliminary PEMFC experiment to assess the corrosion-resistance of our catalyst by submitting a pristine NNMC CL to the same protocol and conditions used for the recording of the polarization curves, but using N<sub>2</sub> as cathode feed instead of air. The resulting current-potential plot is displayed in Figure 5a, and shows that the electrochemical oxidation currents recorded on this NNMC become significant at potentials  $\geq 0.7 \text{ V}$ . Moreover, these oxidative currents appear to also be responsible for the systematic deviation from a  $70 \text{ mV}\cdot\text{dec}^{-1}$  linear slope observed at high potentials in the Tafel plots in Figure 2b,f,d,h, which has been proposed to be a consequence of the ORR-mechanism on NNMCs.<sup>49</sup> To assess this possibility, the currents in the beginning-

of-life, H<sub>2</sub>/Air polarization curve ( $i_{ORR,measured}$ ) were corrected for the oxidative currents in this H<sub>2</sub>/N<sub>2</sub> test ( $i_{oxidation}$ ) using the equation:

$$i_{ORR,corrected} = i_{ORR,measured} - i_{oxidation} \quad (3)$$

yielding a corrected current ( $i_{ORR,corrected}$ ) that, as showcased in Figure 5b, now features a fully linear slope of 70 mV·dec<sup>-1</sup> at all potentials > 0.8 V. As such, this result suggests that the curvature observed in the Tafel plots at high potentials is exclusively caused by the contributions of a simultaneous oxidative process to the overall measured currents. On the other hand, at the current stage we cannot exclusively ascribe this oxidative current to the electro-oxidation of the catalyst to CO<sub>2</sub>. More precisely, if one assumes that all of the oxidative charge in the ‘N<sub>2</sub>-0.8V’ test (accounting to ≈ 33 mAh·cm<sup>-2</sup> – cf. Figure S4d) were to correspond to the oxidation of the carbon in the NNMC to CO<sub>2</sub>, roughly a third of the catalyst’s carbon would have been fully corroded. By comparison, a comparatively smaller loss of ≈ 10 % of the carbon inventory in Pt/C CLs is known to result in the collapse of their porous network and cell failure<sup>50</sup> – a complete loss of performance that is not observed at the end-of-life of the ‘N<sub>2</sub>-0.8V’ protocol, and that suggests that an undetermined fraction of the charge in that test may result from reactions other than the complete oxidation of carbon to CO<sub>2</sub> (e.g., the formation of C-O surface functionalities).

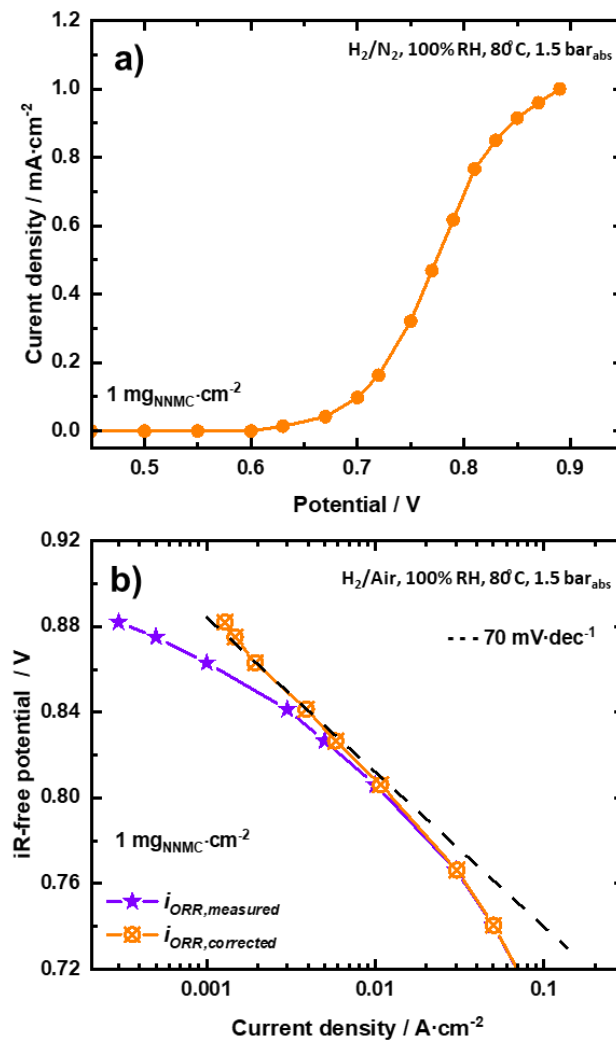


**Figure 5.** Current density vs. potential response recorded in a PEMFC in H<sub>2</sub>/N<sub>2</sub> at 1.5 bar<sub>abs</sub>, 80 °C and 100 % relative humidity using an NNMC cathode loading of 1 mg<sub>NNMC</sub>·cm<sup>-2</sup> (a) and the Tafel plot of the pristine sample recorded in H<sub>2</sub>/Air at 1.5 bar<sub>abs</sub>, 80 °C and 100 % relative humidity with the loading of 1 mg<sub>NNMC</sub>·cm<sup>-2</sup> before and after correcting the measured current with the oxidative current in panel ‘a’ using equation 3 (b).

Having confirmed that the NNMC undergoes an oxidative process at the 0.8 V at which this second set of degradation protocols is carried out, we analyzed the performance decay at

this potential in both the presence and absence of O<sub>2</sub>. The recorded polarization curves and the corresponding Tafel plots are displayed in Figure 2e-h and show that the ‘Air-0.8V’ protocol (expected to entail carbon electro-oxidation together with H<sub>2</sub>O<sub>2</sub>-related effects) leads to drastic performance losses both in the kinetic and high current density regions (whereby the former experienced a  $\approx 95$  % drop with regards to the beginning-of-life value – see Figure 3). In the ‘N<sub>2</sub>-0.8V’ test, however, there was no change in high current density performance, while a  $\approx 60$  % decrease in the ORR activity was determined from the Tafel plot at 0.8 V (see Figure S5 for the ORR activities). This indicates that carbon electro-oxidation alone is highly detrimental to the NNMC’s ORR-activity even in the absence of O<sub>2</sub> and concomitant H<sub>2</sub>O<sub>2</sub>-related effects. It is also worth noting that cyclic voltammograms recorded after these two protocols at 0.8 V featured a slightly larger double layer current (possibly relatable to the corrosion of the carbon<sup>51</sup>) along with a partial disappearance of the redox peaks at  $\approx 0.75$  V present in the CV of the pristine NNMC layer (see Figure S12b). These redox peaks have been correlated to these catalysts’ ORR activity by some studies,<sup>52</sup> but other works have opposed this interpretation.<sup>53</sup> Notably, that lack of redox-peak vs. ORR-activity correlation would also be endorsed by our results, since the CVs of the end-of-life NNMC layers submitted to the protocols at 0.5 V are essentially identical to that of the pristine catalyst (see Figure S12a), even if both CLs suffered from a significant drop of their ORR activity in both tests (i.e.,  $\approx 70$  vs.  $\approx 30$  % losses in ‘Air-0.5V’ vs. ‘N<sub>2</sub>-0.5V’, respectively – see Figure 3). On top of this, we also assessed the effect of this high potential hold on the catalyst’s carbonaceous matrix by performing Raman spectroscopy measurements on pristine and *post mortem* CLs (i.e., prior to and after the ‘N<sub>2</sub>-0.8V’ protocol, respectively). As shown in Fig. S13, the two layers feature almost indistinguishable Raman spectra with a line shape typical of carbon materials submitted to a heat treatment at temperatures  $< 1000$  °C. In the first-order region, the spectra are characterized by two maxima at  $\approx 1350$  and  $\approx 1600$  cm<sup>-1</sup> assigned to the so-called “D” and “G”

lines. In this regard, the intensity of the “D” line and the width of both the “D” and “G” lines clearly indicate that the layers are formed by of a highly defective carbon material with a low average in-plane crystallite size ( $< 2\text{-}3\text{ nm}$ ) and that also contains a high amount of point defects. In such cases, the direct use of the intensity ratio between these lines ( $I_D/I_G$ ) does not allow the determination of the average in-plane crystallite size. However, it is clear that these results do not indicate a massive corrosion of the carbonaceous material, and this is also the case when considering the second-order region of the spectra (not shown here), which also showed no significant changes between pristine and *post mortem* CLs. On the other hand, the results cannot exclude the formation of different carbon-oxygen functionalities that are always very difficult to detect analyzing carbon-based materials. Specifically, this could be regarded as indicative of a C-corrosion mechanism in which the electro-oxidation of the catalyst’s graphene domains leads to an enhancement of their hydrophilicity that in turn causes their dissolution in the aqueous electrolyte, as previously proposed for the electrochemical oxidation of glassy carbon in alkaline medium.<sup>54</sup>

An STEM analysis was also performed on the end-of-life CL submitted to the ‘Air-0.8V’ protocol to assess the morphological and compositional changes caused by this test. As before, F and Fe elemental mapping (Figure S6 f, i), semi-quantitative analysis (Figure S6 j-k) and HAADF imaging and analysis of the Fe agglomerates (Figure S7 c-e) were performed. Similar to the post-mortem CL that had undergone the ‘Air-0.5V’ test, the end-of-life CL after the ‘Air-0.8V’ protocol contained numerous Fe clusters, whose signal did not display an appreciable change compared to that of the pristine CL, and the number and morphology of the Fe agglomerates imaged by HAADF showed no significant changes. As showed by the STEM and XRF measurements carried out on the ‘Air-0.5V’ sample, though, these observations do not rule out a subtle change in the Fe content of the layers; we note in passing that, unfortunately, it was not possible to perform such the time-demanding, synchrotron-assisted

measurements on the *post mortem* ‘Air-0.8V’ sample. On the other hand, the impedance measurements of the end-of-life CLs after the protocols at 0.8 V featured no significant changes in the  $R_{\text{HFR}}$  and  $R_{\text{H}^+, \text{eff}}$  values (with regards to the beginning-of-life) regardless of the cathode feed (see Figure S10c,d and Figure S11). This indicates that, and unlike in the case of the sample submitted to the ‘Air-0.5 V’ protocol (that featured a  $\approx 10\%$  increase of the proton transport resistance), none of these higher potential samples should have suffered from the poisoning of the ionomer by leached Fe-ions discussed above for the lower-potential analogue (i.e., ‘Air-0.5V’). Instead, the  $\text{H}^+$ -conduction properties of the membrane and ionomer in the CL were completely unaffected by the presence or absence of  $\text{O}_2$  in these tests, even if in this case their duration added up to  $\approx 250$  h. Notably, this stability of the ionomer was also confirmed by F-EDS cross-section images of the CLs acquired by STEM, from which no clear differences in fluorine distribution were observed between the pristine CL and the sample submitted to the ‘Air-0.8V’ protocol (Figure S6g, i).

Having discussed all degradation protocols, we now revise the ORR activity losses caused by each of them and plotted in Figure 3. The latter clearly illustrates that the two tests entailing the use of air at the cell’s cathode are unambiguously more detrimental to the ORR-activity than those performed in  $\text{N}_2$ , as already indicated by some recent studies.<sup>27, 30</sup> Interestingly, when one isolates the effects of the potential hold at 0.5 V and of carbon electro-oxidation at 0.8 V based on the extents of degradation observed in the complementing  $\text{N}_2$ -tests (i.e., ‘ $\text{N}_2$ -0.5V’ and ‘ $\text{N}_2$ -0.8V’, respectively), the remaining activity losses in the air protocols and ascribable to  $\text{H}_2\text{O}_2$ -related degradation account for  $\approx 40\%$  of the overall activity decay. This fraction is irrespective of the potential at which these tests were performed, and would therefore imply that these  $\text{H}_2\text{O}_2$ -effects are only dependent of the ORR charge transferred in the course of the test. Such a conclusion would in turn be at odds with the potential-dependent  $\text{H}_2\text{O}_2$ -yields generally observed for NNMCs in the rotating ring disk electrode (RRDE)

experiments customarily used to assess their ORR-selectivity.<sup>55</sup> This contradiction could stem from the significant differences between the testing environments in these RRDE tests and actual PEMFC MEAs (e.g., liquid vs. solid electrolyte, different mass transport limitations, etc.), which has been widely discussed in the literature in the specific context of Pt-based catalyst<sup>56</sup> and also observed for NNMCs.<sup>57</sup> As for the results observed in the tests using N<sub>2</sub> at the cathode, the smaller ORR-activity losses observed in the protocol at 0.5 V vs. 0.8 V imply that carbon electro-oxidation at the latter potential is more detrimental to the ORR-activity than the Fe-demetalation caused by the former, even if the effects of that test at 0.5 V were by no means negligible.

To finalize this study, we delve in the effects of the different stability tests and corresponding degradation mechanisms on the mass transport properties of these CLs. To this end, the mass transport overpotentials ( $\eta_{tx}$ s) of the pristine CL and of the CLs submitted to each of the degradation protocols were estimated from the potential difference between the extrapolated Tafel lines and the polarization curves corrected for all ohmic losses (i.e.,  $R_{HFR}$  and  $R_{H^+,cathode}^{eff}$ ), and displayed in Figure S14. Figure 6 then features the change in mass transport overpotential ( $\Delta\eta_{tx}$ ) inferred by each testing condition, which was calculated as the difference between the  $\eta_{tx}$  of the pristine CL and that of each end-of-life sample (i.e.,  $\eta_{pristine} - \eta_{post-mortem}$ ), in all cases at a current of 0.8 A·cm<sup>-2</sup> (see Figure S15). The results in Figure 6 indicate that the mass transport worsened after the two protocols performed in air, in which the increase in  $\eta_{tx}$  qualitatively scales with the loss of the kinetic activity (see Figure 3). In other words, the increase in the  $\eta_{tx}$  was  $\approx 25$  mV larger in the post-mortem sample submitted to the ‘Air-0.8V’ protocol, for which the ORR-activity loss was also higher compared to sample submitted to the ‘Air-0.5V’ protocol ( $\approx 95$  vs.  $\approx 70$  % with regards to the beginning-of-life value, respectively). This observation qualitatively confirms the correlation between the number of ORR-active sites in this type of NNMC and its CLs’ mass transport (whereby more

vs. less sites imply a lower / higher  $\eta_{tx}$  value) postulated in our recent work,<sup>32</sup> and originally reported for Pt-based ORR-catalyst.<sup>11</sup> Additionally, in the case of the ‘Air-0.8V’ test, the electro-oxidation of the catalyst’s surface expected at high potential is known to increase the hydrophilicity of the CL, further worsening its mass transport properties. In the case of both N<sub>2</sub> protocols, however, the mass transport properties of the end-of-life CLs systematically improved when compared to the pristine sample. For the N<sub>2</sub>-test at a low potential of 0.5 V, this improvement can be attributed to the potential-driven reduction of the catalyst’s surface (e.g., hydroquinone groups),<sup>26</sup> which would entail the removal of hydrophilic O-functionalities and increase the CL’s hydrophobicity, thus leading to a better water management. On the other hand, the enhancement of the mass transport observed for the CL having undergone the N<sub>2</sub>-protocol at 0.8 V is more puzzling, since we would expect that the above discussed electro-oxidation of the carbon surface at this high potential would increase the CL’s hydrophilicity and worsen its mass transport properties. We hypothesize that this effect may be counteracted by localized C-electro-oxidation to CO<sub>2</sub>, which may expose more graphitic (and thus hydrophobic) domains and eventually lead to an additional re-distribution of the ionomer that may lead to a net improvement in mass transport along this CL.

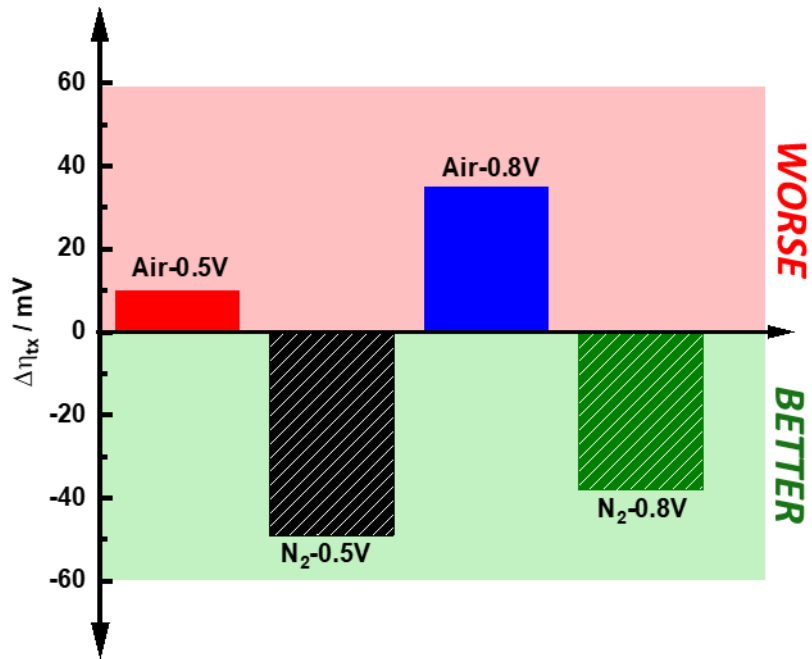


**Figure 6.** Summary of the changes in mass transport overpotential ( $\Delta\eta_{tx} = \eta_{\text{pristine}} - \eta_{\text{post-mortem}}$ ) after each degradation protocols, whereby red- vs. green-shaded areas represent worse vs. better mass transport properties, respectively.

## CONCLUSIONS

In this study, we aimed to disentangle the relative contributions to the overall PEMFC-performance losses of the three main NNMC-deactivation paths proposed in the literature (i.e., demetallation, electrochemical carbon oxidation and H<sub>2</sub>O<sub>2</sub>-related effects) by using four degradation protocols implying different cathode gas feeds (i.e., air vs. N<sub>2</sub>), potential holds and durations. Our results indicated that H<sub>2</sub>O<sub>2</sub>-effects on the catalyst's ORR-activity appear to depend only on the ORR-charge, and not on the test's operative potential. Interestingly, the chemical degradation of the ionomer and/or membrane that might originate from H<sub>2</sub>O<sub>2</sub>-derived species does not seem to significantly contribute to the performance decay observed under air operation, at least within the duration of protocols presented here. Complementarily, we found that electrochemical carbon oxidation in the protocols at a higher potential of 0.8 V contributes to the ORR-activity loss more significantly than Fe-demetalation at 0.5 V, even if the effect of the latter mechanism was not negligible. Notably, this observation is likely to be highly dependent on the potentials chosen for these tests, since demetallation vs. C-oxidation are expected to be exacerbated as the potential decreases or increases, respectively.<sup>13, 14</sup> Moreover, the CLs' mass transport properties worsened after both of the protocols performed using air at the cathode, and the observed increase of the  $\eta_{tx}$  qualitatively matched with the extent of ORR activity loss. On the other hand, the mass transport systematically improved after the protocols performed under N<sub>2</sub> both at 0.5 and 0.8 V; the former potential possibly implies a reduction of the catalyst's surface that would enhance the CL's hydrophobicity leading to this decreased  $\eta_{tx}$ , while the reason for the improvement obtained in the 0.8 V protocol remains unclear.

We believe that the combination of durability tests presented herein can help to differentiate and quantify the impact of these degradation mechanisms on NNMCs' stability. Specifically, the combined protocols may prove extremely useful for comparing catalysts with well-established metal speciations (e.g., Co vs. Fe-based, featuring other single atom vs. metal NP

ratios) and physicochemical features (e.g., surface composition, carbon graphitization extent), as it could serve to establish ties between these properties and the relative impact of different instability mechanisms. The knowledge gained through such comparisons could in turn be used to guide the design of NNMCs with the sufficiently high durability required for their implementation in commercial PEMFCs.

## **ASSOCIATED CONTENT**

### **Supporting Information.**

## **AUTHOR INFORMATION**

### **Corresponding Author**

\*Juan Herranz (email: [juan.herranz@psi.ch](mailto:juan.herranz@psi.ch))

### **Author Contributions**

The manuscript was written through contributions of all authors. All authors have given approval to the final version of the manuscript.

### **Funding Sources**

S.Ü., R.G., V.S., T.J.S. and J.H. gratefully acknowledge funding from the Swiss National Science Foundation, under the funding scheme Sinergia (project grant number 180335). C.A. has received funding from the European Union's Horizon 2020 research and innovation programme under the Marie Skłodowska-Curie grant agreement No 884104. C.A. is also supported by funding from Chalmers's initiative for advancement of neutron and X-ray techniques.

### **Notes**

The authors declare no competing financial interest.

## **ACKNOWLEDGMENT**

We would like to thank the staff of the beamline ID16A-NI at the European Synchrotron Radiation Facility (ESRF), Grenoble, France for providing beamtime for nano-XRF imaging

experiments under the proposal number MA-5294. For the nano-XRF sample preparation, we also acknowledge the ScopeM staff at ETH Zurich: Joakim Reuteler and Stephan Handschin for embedding and Eszter Barthazy for microtome cutting. We are also grateful to Dr. Jinzhen Huang for his help with the XRD measurements.

## REFERENCES

- (1) International Energy Agency's CO<sub>2</sub> emissions from fuel combustion highlights **2020**.
- (2) Eberle, U.; Müller, B.; von Helmlolt, R. Fuel cell electric vehicles and hydrogen infrastructure: status 2012. *Energy & Environmental Science* **2012**, *5* (10). DOI: 10.1039/c2ee22596d.
- (3) Staffell, I.; Scamman, D.; Velazquez Abad, A.; Balcombe, P.; Dodds, P. E.; Ekins, P.; Shah, N.; Ward, K. R. The role of hydrogen and fuel cells in the global energy system. *Energy & Environmental Science* **2019**, *12* (2), 463-491. DOI: 10.1039/c8ee01157e. Wagner, F. T.; Lakshmanan, B.; Mathias, M. F. Electrochemistry and the Future of the Automobile. *The Journal of Physical Chemistry Letters* **2010**, *1* (14), 2204-2219. DOI: 10.1021/jz100553m. Gröger, O.; Gasteiger, H. A.; Suchsland, J.-P. Review—Electromobility: Batteries or Fuel Cells? *Journal of The Electrochemical Society* **2015**, *162* (14), A2605-A2622. DOI: 10.1149/2.0211514jes. Cano, Z. P.; Banham, D.; Ye, S.; Hintennach, A.; Lu, J.; Fowler, M.; Chen, Z. Batteries and fuel cells for emerging electric vehicle markets. *Nature Energy* **2018**, *3* (4), 279-289. DOI: 10.1038/s41560-018-0108-1. Cullen, D. A.; Neyerlin, K. C.; Ahluwalia, R. K.; Mukundan, R.; More, K. L.; Borup, R. L.; Weber, A. Z.; Myers, D. J.; Kusoglu, A. New roads and challenges for fuel cells in heavy-duty transportation. *Nature Energy* **2021**, *6* (5), 462-474. DOI: 10.1038/s41560-021-00775-z.
- (4) Thompson, S. T.; Papageorgopoulos, D. Platinum group metal-free catalysts boost cost competitiveness of fuel cell vehicles. *Nature Catalysis* **2019**, *2* (7), 558-561. DOI: 10.1038/s41929-019-0291-x.

(5) Sahraie, N. R.; Kramm, U. I.; Steinberg, J.; Zhang, Y.; Thomas, A.; Reier, T.; Paraknowitsch, J. P.; Strasser, P. Quantifying the density and utilization of active sites in non-precious metal oxygen electroreduction catalysts. *Nat Commun* **2015**, *6*, 8618. DOI: 10.1038/ncomms9618.

(6) Ferrandon, M.; Wang, X.; Kropf, A. J.; Myers, D. J.; Wu, G.; Johnston, C. M.; Zelenay, P. Stability of iron species in heat-treated polyaniline–iron–carbon polymer electrolyte fuel cell cathode catalysts. *Electrochimica Acta* **2013**, *110*, 282-291. DOI: 10.1016/j.electacta.2013.03.183. Herranz, J.; Jaouen, F.; Lefevre, M.; Kramm, U. I.; Proietti, E.; Dodelet, J. P.; Bogdanoff, P.; Fiechter, S.; Abs-Wurmbach, I.; Bertrand, P.; et al. Unveiling N-protonation and anion-binding effects on Fe/N/C-catalysts for O<sub>2</sub> reduction in PEM fuel cells. *J Phys Chem C Nanomater Interfaces* **2011**, *115* (32). DOI: 10.1021/jp2042526 From NLM PubMed-not-MEDLINE. Ebner, K.; Clark, A. H.; Saveleva, V. A.; Smolentsev, G.; Chen, J.; Ni, L.; Li, J.; Zitolo, A.; Jaouen, F.; Kramm, U. I.; et al. Time-Resolved Potential-Induced Changes in Fe/N/C-Catalysts Studied by In Situ Modulation Excitation X-Ray Absorption Spectroscopy. *Advanced Energy Materials* **2022**, *12* (14). DOI: 10.1002/aenm.202103699. Ni, L.; Gallenkamp, C.; Paul, S.; Kübler, M.; Theis, P.; Chhabra, S.; Hofmann, K.; Bill, E.; Schnegg, A.; Albert, B.; et al. Active Site Identification in FeNC Catalysts and Their Assignment to the Oxygen Reduction Reaction Pathway by In Situ <sup>57</sup>Fe Mössbauer Spectroscopy. *Advanced Energy and Sustainability Research* **2021**, *2* (2), 2000064. DOI: 10.1002/aesr.202000064. Ni, L.; Gallenkamp, C.; Wagner, S.; Bill, E.; Krewald, V.; Kramm, U. I. Identification of the Catalytically Dominant Iron Environment in Iron- and Nitrogen-Doped Carbon Catalysts for the Oxygen Reduction Reaction. *J Am Chem Soc* **2022**, *144* (37), 16827. DOI: 10.1021/jacs.2c04865 From NLM PubMed-not-MEDLINE. Kramm, U. I.; Herranz, J.; Larouche, N.; Arruda, T. M.; Lefevre, M.; Jaouen, F.; Bogdanoff, P.; Fiechter, S.; Abs-Wurmbach, I.; Mukerjee, S.; et al. Structure of the catalytic sites in Fe/N/C-

catalysts for O<sub>2</sub>-reduction in PEM fuel cells. *Phys Chem Chem Phys* **2012**, *14* (33), 11673-11688. DOI: 10.1039/c2cp41957b. Chung, H. T.; Cullen, D. A.; Higgins, D.; Sneed, B. T.; Holby, E. F.; More, K. L.; Zelenay, P. Direct atomic-level insight into the active sites of a high-performance PGM-free ORR catalyst. *Science* **2017**, *357*, 479-484.

(7) Li, J.; Sougrati, M. T.; Zitolo, A.; Ablett, J. M.; Oğuz, I. C.; Mineva, T.; Matanovic, I.; Atanassov, P.; Huang, Y.; Zenyuk, I.; et al. Identification of durable and non-durable FeN<sub>x</sub> sites in Fe–N–C materials for proton exchange membrane fuel cells. *Nature Catalysis* **2021**, *4* (1), 10-19. DOI: 10.1038/s41929-020-00545-2.

(8) Ebner, K.; Herranz, J.; Saveleva, V. A.; Kim, B.-J.; Henning, S.; Demicheli, M.; Krumeich, F.; Nachtegaal, M.; Schmidt, T. J. Fe-Based O<sub>2</sub>-Reduction Catalysts Synthesized Using Na<sub>2</sub>CO<sub>3</sub> as a Pore-Inducing Agent. *ACS Applied Energy Materials* **2019**, *2* (2), 1469-1479. DOI: 10.1021/acsaem.8b02036. Iwase, K.; Ebner, K.; Diercks, J. S.; Saveleva, V. A.; Unsal, S.; Krumeich, F.; Harada, T.; Honma, I.; Nakanishi, S.; Kamiya, K.; et al. Effect of Cobalt Speciation and the Graphitization of the Carbon Matrix on the CO<sub>2</sub> Electroreduction Activity of Co/N-Doped Carbon Materials. *ACS Appl Mater Interfaces* **2021**, *13* (13), 15122-15131. DOI: 10.1021/acsaem.8b02036 From NLM PubMed-not-MEDLINE.

(9) Ebner, K.; Ni, L.; Saveleva, V. A.; Le Monnier, B. P.; Clark, A. H.; Krumeich, F.; Nachtegaal, M.; Luterbacher, J. S.; Kramm, U. I.; Schmidt, T. J.; et al. (57)Fe-Enrichment effect on the composition and performance of Fe-based O<sub>2</sub>-reduction electrocatalysts. *Phys Chem Chem Phys* **2021**, *23* (15), 9147-9157. DOI: 10.1039/d1cp00707f.

(10) Varnell, J. A.; Tse, E. C. M.; Schulz, C. E.; Fister, T. T.; Haasch, R. T.; Timoshenko, J.; Frenkel, A. I.; Gewirth, A. A. Identification of carbon-encapsulated iron nanoparticles as active species in non-precious metal oxygen reduction catalysts. *Nature Communications* **2016**, *7* (1). DOI: 10.1038/ncomms12582.

- (11) Kongkanand, A.; Mathias, M. F. The Priority and Challenge of High-Power Performance of Low-Platinum Proton-Exchange Membrane Fuel Cells. *J Phys Chem Lett* **2016**, *7* (7), 1127-1137. DOI: 10.1021/acs.jpcclett.6b00216.
- (12) Banham, D.; Ye, S.; Pei, K.; Ozaki, J.-i.; Kishimoto, T.; Imashiro, Y. A review of the stability and durability of non-precious metal catalysts for the oxygen reduction reaction in proton exchange membrane fuel cells. *Journal of Power Sources* **2015**, *285*, 334-348. DOI: 10.1016/j.jpowsour.2015.03.047.
- (13) Choi, C. H.; Baldizzone, C.; Grote, J. P.; Schuppert, A. K.; Jaouen, F.; Mayrhofer, K. J. Stability of Fe-N-C Catalysts in Acidic Medium Studied by Operando Spectroscopy. *Angew Chem Int Ed Engl* **2015**, *54* (43), 12753-12757. DOI: 10.1002/anie.201504903.
- (14) Choi, C. H.; Baldizzone, C.; Polymeros, G.; Pizzutilo, E.; Kasian, O.; Schuppert, A. K.; Ranjbar Sahraie, N.; Sougrati, M.-T.; Mayrhofer, K. J. J.; Jaouen, F. Minimizing Operando Demetallation of Fe-N-C Electrocatalysts in Acidic Medium. *ACS Catalysis* **2016**, *6* (5), 3136-3146. DOI: 10.1021/acscatal.6b00643.
- (15) Glibin, V. P.; Dodelet, J.-P. Thermodynamic Stability in Acid Media of FeN<sub>4</sub>-Based Catalytic Sites Used for the Reaction of Oxygen Reduction in PEM Fuel Cells. *Journal of The Electrochemical Society* **2017**, *164* (9), F948-F957. DOI: 10.1149/2.1041709jes. Dobrota, A. S.; Skorodumova, N. V.; Mentus, S. V.; Pašti, I. A. Surface pourbaix plots of M@N<sub>4</sub>-graphene single-atom electrocatalysts from density functional theory thermodynamic modeling. *Electrochimica Acta* **2022**, *412*. DOI: 10.1016/j.electacta.2022.140155.
- (16) Sun, F.; Li, F.; Tang, Q. Spin State as a Participator for Demetalation Durability and Activity of Fe–N–C Electrocatalysts. *The Journal of Physical Chemistry C* **2022**, *126* (31), 13168-13181. DOI: 10.1021/acs.jpcc.2c03518.
- (17) Holby, E. F.; Wang, G.; Zelenay, P. Acid Stability and Demetalation of PGM-Free ORR Electrocatalyst Structures from Density Functional Theory: A Model for “Single-Atom

Catalyst” Dissolution. *ACS Catalysis* **2020**, *10* (24), 14527-14539. DOI: 10.1021/acscatal.0c02856.

(18) Chenitz, R.; Kramm, U. I.; Lefèvre, M.; Glibin, V.; Zhang, G.; Sun, S.; Dodelet, J.-P. A specific demetalation of Fe–N<sub>4</sub> catalytic sites in the micropores of NC\_Ar + NH<sub>3</sub> is at the origin of the initial activity loss of the highly active Fe/N/C catalyst used for the reduction of oxygen in PEM fuel cells. *Energy & Environmental Science* **2018**, *11* (2), 365-382. DOI: 10.1039/c7ee02302b.

(19) Chen, J.; Yan, X.; Fu, C.; Feng, Y.; Lin, C.; Li, X.; Shen, S.; Ke, C.; Zhang, J. Insight into the Rapid Degradation Behavior of Nonprecious Metal Fe-N-C Electrocatalyst-Based Proton Exchange Membrane Fuel Cells. *ACS Appl Mater Interfaces* **2019**, *11* (41), 37779-37786. DOI: 10.1021/acсами.9b13474 From NLM PubMed-not-MEDLINE.

(20) Kangasniemi, K. H.; Condit, D. A.; Jarvic, T. D. Characterization of Vulcan Electrochemically Oxidized under Simulated PEM Fuel Cell Conditions. *Journal of The Electrochemical Society* **2004**, *151* (4), E125-E132. DOI: DOI: 10.1149/1.1649756.

(21) Wang, Y.-C.; Zhu, P.-F.; Yang, H.; Huang, L.; Wu, Q.-H.; Rauf, M.; Zhang, J.-Y.; Dong, J.; Wang, K.; Zhou, Z.-Y.; et al. Surface Fluorination to Boost the Stability of the Fe/N/C Cathode in Proton Exchange Membrane Fuel Cells. *ChemElectroChem* **2018**, *5* (14), 1914-1921. DOI: 10.1002/celc.201700939.

(22) Zhang, G.; Chenitz, R.; Lefèvre, M.; Sun, S.; Dodelet, J.-P. Is iron involved in the lack of stability of Fe/N/C electrocatalysts used to reduce oxygen at the cathode of PEM fuel cells? *Nano Energy* **2016**, *29*, 111-125. DOI: 10.1016/j.nanoen.2016.02.038.

(23) Martinaiou, I.; Shahraei, A.; Grimm, F.; Zhang, H.; Wittich, C.; Klemenz, S.; Dolique, S. J.; Kleebe, H.-J.; Stark, R. W.; Kramm, U. I. Effect of metal species on the stability of Me-N-C catalysts during accelerated stress tests mimicking the start-up and shut-down conditions. *Electrochimica Acta* **2017**, *243*, 183-196. DOI: 10.1016/j.electacta.2017.04.134.

- (24) Avasarala, B.; Moore, R.; Haldar, P. Surface oxidation of carbon supports due to potential cycling under PEM fuel cell conditions. *Electrochimica Acta* **2010**, *55* (16), 4765-4771. DOI: 10.1016/j.electacta.2010.03.056. Castanheira, L.; Dubau, L.; Mermoux, M.; Berthomé, G.; Caqué, N.; Rossinot, E.; Chatenet, M.; Maillard, F. Carbon Corrosion in Proton-Exchange Membrane Fuel Cells: From Model Experiments to Real-Life Operation in Membrane Electrode Assemblies. *ACS Catalysis* **2014**, *4* (7), 2258-2267. DOI: 10.1021/cs500449q.
- (25) LaConti, A. B.; Mamdan, M.; McDonald, R. C. In *Handbook of Fuel Cells: Fundamentals, Technology and Applications*, Vielstich, W., Lamm, A., Gasteiger, H. A., Yokokawa, H. Eds.; Vol. 3; John Wiley & Sons 2003; p 648. Gubler, L.; Dockheer, S. M.; Koppenol, W. H. Radical (HO•, H• and HOO•) Formation and Ionomer Degradation in Polymer Electrolyte Fuel Cells. *Journal of The Electrochemical Society* **2011**, *158* (7), B755-B769. DOI: 10.1149/1.3581040.
- (26) Choi, C. H.; Lim, H.-K.; Chung, M. W.; Chon, G.; Ranjbar Sahraie, N.; Altin, A.; Sougrati, M.-T.; Stievano, L.; Oh, H. S.; Park, E. S.; et al. The Achilles' heel of iron-based catalysts during oxygen reduction in an acidic medium. *Energy & Environmental Science* **2018**, *11* (11), 3176-3182. DOI: 10.1039/c8ee01855c.
- (27) Kumar, K.; Dubau, L.; Mermoux, M.; Li, J.; Zitolo, A.; Nelayah, J.; Jaouen, F.; Maillard, F. On the Influence of Oxygen on the Degradation of Fe-N-C Catalysts. *Angew Chem Int Ed Engl* **2020**, *59* (8), 3235-3243. DOI: 10.1002/anie.201912451.
- (28) Ferreira, P. J.; la O', G. J.; Shao-Horn, Y.; Morgan, D.; Makharia, R.; Kocha, S.; Gasteiger, H. A. Instability of Pt/C Electrocatalysts in Proton Exchange Membrane Fuel Cells. *Journal of The Electrochemical Society* **2005**, *152* (11), A2256-A2271. DOI: 10.1149/1.2050347. Shao-Horn, Y.; Sheng, W. C.; Chen, S.; Ferreira, P. J.; Holby, E. F.; Morgan, D. Instability of Supported Platinum Nanoparticles in Low-Temperature Fuel Cells. *Topics in Catalysis* **2007**, *46* (3-4), 285-305. DOI: 10.1007/s11244-007-9000-0.

- (29) Castanheira, L.; Silva, W. O.; Lima, F. H. B.; Crisci, A.; Dubau, L.; Maillard, F. Carbon Corrosion in Proton-Exchange Membrane Fuel Cells: Effect of the Carbon Structure, the Degradation Protocol, and the Gas Atmosphere. *ACS Catalysis* **2015**, *5* (4), 2184-2194. DOI: 10.1021/cs501973j. Stariha, S.; Macauley, N.; Sneed, B. T.; Langlois, D.; More, K. L.; Mukundan, R.; Borup, R. L. Recent Advances in Catalyst Accelerated Stress Tests for Polymer Electrolyte Membrane Fuel Cells. *Journal of The Electrochemical Society* **2018**, *165* (7), F492-F501. DOI: 10.1149/2.0881807jes.
- (30) Zhang, H.; Osmieri, L.; Park, J. H.; Chung, H. T.; Cullen, D. A.; Neyerlin, K. C.; Myers, D. J.; Zelenay, P. Standardized protocols for evaluating platinum group metal-free oxygen reduction reaction electrocatalysts in polymer electrolyte fuel cells. *Nature Catalysis* **2022**, *5* (5), 455-462. DOI: 10.1038/s41929-022-00778-3.
- (31) Ünsal, S.; Schmidt, T. J.; Herranz, J. Effect of Aggregate Size and Film Quality on the Electrochemical Properties of Non-noble Metal Catalysts in Rotating Ring Disk Electrode Measurements. *Electrochimica Acta* **2023**, *445*. DOI: 10.1016/j.electacta.2023.142024.
- (32) Ünsal, S.; Bozzetti, M.; Chen, Y.-C.; Girod, R.; Berger, A.; Diercks, J. S.; Gialamoidou, S.; Lyu, J.; Medarde, M.; Gasteiger, H. A.; et al. Catalyst Aggregate Size Effect on the Mass Transport Properties of Non-Noble Metal Catalyst Layers for PEMFC Cathodes. *ACS Applied Material Interfaces* **2022**, *submitted*.
- (33) Yin, X.; Lin, L.; Chung, H. T.; Komini Babu, S.; Martinez, U.; Purdy, G. M.; Zelenay, P. Effects of MEA Fabrication and Ionomer Composition on Fuel Cell Performance of PGM-free ORR Catalyst. *ECS Transactions* **2017**, *77* (11), 1273-1281
- (34) Oberholzer, P.; Boillat, P. Local Characterization of PEFCs by Differential Cells: Systematic Variations of Current and Asymmetric Relative Humidity. *Journal of The Electrochemical Society* **2014**, *161* (1), F139-F152. DOI: 10.1149/2.080401jes.

- (35) Liu, Y.; Murphy, M. W.; Baker, D. R.; Gu, W.; Ji, C.; Jorne, J.; Gasteiger, H. A. Proton Conduction and Oxygen Reduction Kinetics in PEM Fuel Cell Cathodes: Effects of Ionomer-to-Carbon Ratio and Relative Humidity. *Journal of The Electrochemical Society* **2009**, *156* (8). DOI: 10.1149/1.3143965.
- (36) Neyerlin, K. C.; Gu, W.; Jorne, J.; Clark, A.; Gasteiger, H. A. Cathode Catalyst Utilization for the ORR in a PEMFC. *Journal of The Electrochemical Society* **2007**, *154* (2). DOI: 10.1149/1.2400626.
- (37) Neyerlin, K. C.; Gu, W.; Jorne, J.; Gasteiger, H. A. Study of the Exchange Current Density for the Hydrogen Oxidation and Evolution Reactions. *Journal of The Electrochemical Society* **2007**, *154* (7). DOI: 10.1149/1.2733987.
- (38) Bernardi, D. M.; Verbrugge, M. V. A Mathematical Model of the Solid-Polymer-Electrolyte Fuel Cell. *Journal of Electrochemical Society* **1992**, *139*, 2477.
- (39) Holler, M.; Raabe, J.; Wepf, R.; Shahmoradian, S. H.; Diaz, A.; Sarafimov, B.; Lachat, T.; Walther, H.; Vitins, M. OMNY PIN-A versatile sample holder for tomographic measurements at room and cryogenic temperatures. *Rev Sci Instrum* **2017**, *88* (11), 113701. DOI: 10.1063/1.4996092 From NLM PubMed-not-MEDLINE.
- (40) Holler, M.; Ihli, J.; Tsai, E. H. R.; Nudelman, F.; Verezhak, M.; van de Berg, W. D. J.; Shahmoradian, S. H. A lathe system for micrometre-sized cylindrical sample preparation at room and cryogenic temperatures. *J Synchrotron Radiat* **2020**, *27* (Pt 2), 472-476. DOI: 10.1107/S1600577519017028 From NLM PubMed-not-MEDLINE.
- (41) Berg, S.; Kutra, D.; Kroeger, T.; Straehle, C. N.; Kausler, B. X.; Haubold, C.; Schiegg, M.; Ales, J.; Beier, T.; Rudy, M.; et al. ilastik: interactive machine learning for (bio)image analysis. *Nat Methods* **2019**, *16* (12), 1226-1232. DOI: 10.1038/s41592-019-0582-9 From NLM Medline.

- (42) Legland, D.; Arganda-Carreras, I.; Andrey, P. MorphoLibJ: integrated library and plugins for mathematical morphology with ImageJ. *Bioinformatics* **2016**, *32* (22), 3532-3534. DOI: 10.1093/bioinformatics/btw413 From NLM Medline.
- (43) Dempster, A. P.; Laird, N. M.; Rubin, D. B. Maximum Likelihood from Incomplete Data via the EM Algorithm. *Journal of the Royal Statistical Society, Series B* **1977**, *39* (1), 1-38.
- (44) Clark, A. H.; Steiger, P.; Bornmann, B.; Hitz, S.; Frahm, R.; Ferri, D.; Nachtegaal, M. Fluorescence-detected quick-scanning X-ray absorption spectroscopy. *Journal of Synchrotron Radiation* **2020**, *27* (Pt 3), 681-688. DOI: 10.1107/S1600577520002350.
- (45) Clark, A. H.; Imbao, J.; Frahm, R.; Nachtegaal, M. ProQEXAFS: a highly optimized parallelized rapid processing software for QEXAFS data. *Journal of Synchrotron Radiation* **2020**, *27* (Pt 2), 551-557. DOI: 10.1107/S1600577519017053.
- (46) Ravel, B.; Newville, M. ATHENA, ARTEMIS, HEPHAESTUS: data analysis for X-ray absorption spectroscopy using IFEFFIT. *Journal of Synchrotron Radiation* **2005**, *12* (Pt 4), 537-541. DOI: 10.1107/S0909049505012719.
- (47) Ebner, K. Fe/N/C-type Oxygen Reduction Reaction Catalysts From Synthesis to Advanced In Situ Spectroscopic Characterization. ETH Zurich, 2020.
- (48) Strickland, K.; Miner, E.; Jia, Q.; Tylus, U.; Ramaswamy, N.; Liang, W.; Sougrati, M. T.; Jaouen, F.; Mukerjee, S. Highly active oxygen reduction non-platinum group metal electrocatalyst without direct metal-nitrogen coordination. *Nat Commun* **2015**, *6*, 7343. DOI: 10.1038/ncomms8343.
- (49) Chlistunoff, J. RRDE and Voltammetric Study of ORR on Pyrolyzed Fe/Polyaniline Catalyst. On the Origins of Variable Tafel Slopes. *The Journal of Physical Chemistry C* **2011**, *115* (14), 6496-6507. DOI: 10.1021/jp108350t.
- (50) Gasteiger, H. A.; Gu, W.; Litterer, B.; Makharia, R.; B., B.; Budinski, M.; Thompson, E.; Wagner, F. T.; Yan, S. G.; Yu, P. T. Catalyst Degradation Mechanisms in PEM and Direct

- Methanol Fuel Cells. In *Mini-Micro Fuel Cells. NATO Science for Peace and Security Series C: Environmental Security*, Kakaç, S., Pramuanjaroenkij, A., Vasiliev, L. Eds.; Springer, 2008.
- (51) Povia, M.; Herranz, J.; Binniger, T.; Nachtegaal, M.; Diaz, A.; Kohlbrecher, J.; Abbott, D. F.; Kim, B.-J.; Schmidt, T. J. Combining SAXS and XAS To Study the Operando Degradation of Carbon-Supported Pt-Nanoparticle Fuel Cell Catalysts. *ACS Catalysis* **2018**, *8* (8), 7000-7015. DOI: 10.1021/acscatal.8b01321.
- (52) Tylus, U.; Jia, Q.; Strickland, K.; Ramaswamy, N.; Serov, A.; Atanassov, P.; Mukerjee, S. Elucidating Oxygen Reduction Active Sites in Pyrolyzed Metal-Nitrogen Coordinated Non-Precious-Metal Electrocatalyst Systems. *J Phys Chem C Nanomater Interfaces* **2014**, *118* (17), 8999-9008. DOI: 10.1021/jp500781v. Osmieri, L.; Ahluwalia, R. K.; Wang, X.; Chung, H. T.; Yin, X.; Kropf, A. J.; Park, J.; Cullen, D. A.; More, K. L.; Zelenay, P.; et al. Elucidation of Fe-N-C electrocatalyst active site functionality via in-situ X-ray absorption and operando determination of oxygen reduction reaction kinetics in a PEFC. *Applied Catalysis B: Environmental* **2019**, *257*. DOI: 10.1016/j.apcatb.2019.117929.
- (53) Elvington, M. C.; Chung, H. T.; Lin, L.; Yin, X.; Ganesan, P.; Zelenay, P.; Colón-Mercado, H. R. Communication—On the Lack of Correlation between the Voltammetric Redox Couple and ORR Activity of Fe-N-C Catalysts. *Journal of The Electrochemical Society* **2020**, *167* (13). DOI: 10.1149/1945-7111/abb97c.
- (54) Yi, Y.; Weinberg, G.; Prenzel, M.; Greiner, M.; Heumann, S.; Becker, S.; Schlögl, R. Electrochemical corrosion of a glassy carbon electrode. *Catalysis Today* **2017**, *295*, 32-40. DOI: 10.1016/j.cattod.2017.07.013.
- (55) Primbs, M.; Sun, Y.; Roy, A.; Malko, D.; Mehmood, A.; Sougrati, M.-T.; Blanchard, P.-Y.; Granozzi, G.; Kosmala, T.; Daniel, G.; et al. Establishing reactivity descriptors for platinum group metal (PGM)-free Fe-N-C catalysts for PEM fuel cells. *Energy & Environmental Science* **2020**, *13* (8), 2480-2500. DOI: 10.1039/d0ee01013h. Bonakdarpour, A.; Lefevre, M.;

Yang, R.; Jaouen, F.; Dahn, T.; Dodelet, J.-P.; Dahn, J. R. Impact of Loading in RRDE Experiments on Fe–N–C Catalysts: Two- or Four-Electron Oxygen Reduction? *Electrochemical and Solid-State Letters* **2008**, *11* (6), B105-B108. DOI: 10.1149/1.2904768.

(56) Lazaridis, T.; Stühmeier, B. M.; Gasteiger, H. A.; El-Sayed, H. A. Capabilities and limitations of rotating disk electrodes versus membrane electrode assemblies in the investigation of electrocatalysts. *Nature Catalysis* **2022**, *5* (5), 363-373. DOI: 10.1038/s41929-022-00776-5.

(57) Jaouen, F.; Goellner, V.; Lefèvre, M.; Herranz, J.; Proietti, E.; Dodelet, J. P. Oxygen reduction activities compared in rotating-disk electrode and proton exchange membrane fuel cells for highly active FeNC catalysts. *Electrochimica Acta* **2013**, *87*, 619-628. DOI: 10.1016/j.electacta.2012.09.057.